Journal of
Composites Science

MDPI

Article

Multifunctional Ag Nanoparticles and Ag/Jute Nanocomposites Derived from *Erythroxylum coca* Tea Waste for Antimicrobial Activity and Single/Multicomponent Catalytic Pollutant Degradation

Yeshua Díaz Zamora [1], Mateo Burke Irazoque [2], Carla Calderón Toledo [2], Sergio Gutiérrez Cortez [2], Alien Blanco Flores [3,*], Delfino Reyes Contreras [4,*], Miguel A. Camacho López [5], Helen Paola Toledo Jaldin [4], Delia Monserrat Ávila Márquez [4] and Alfredo Rafael Vilchis Néstor [6]

1 Master's Program in Materials Science, School of Chemistry, Autonomous University of the State of Mexico, Santiago Tianguistenco 52650, Mexico; ydiaz@ylpet.com.mx
2 Environmental Microbiology Unit, Institute of Molecular Biology and Biotechnology (IBMB), Universidad Mayor de San Andrés, La Paz 0201-0220, Bolivia; mburkei2@fcpn.edu.bo (M.B.I.); cvcalderon@fcpn.edu.bo (C.C.T.); sgutierrezc@fcpn.edu.bo (S.G.C.)
3 National Technological of Mexico, Technological of Superior Studies of Tianguistenco, Mechanical Engineering Division, Santiago Tianguistenco 52650, Mexico
4 Laboratory of Optoacoustics and Nanomaterials (LOAN), School of Sciences, "El Cerrillo" Campus, Autonomous University of the State of Mexico, Toluca 50200, Mexico; helen_mecanica@test.edu.mx (H.P.T.J.); deliam_am@test.edu.mx (D.M.Á.M.)
5 Laboratory of Photomedicine, Biophotonics, and Ultrashort Pulse Laser Spectroscopy, School of Medicine, Autonomous University of the State of Mexico, Toluca 50180, Mexico; macamachol@uaemex.mx
6 Joint Center for Research in Sustainable Chemistry, Autonomous University of the State of Mexico (UAEM)-National Autonomous University of Mexico (UNAM), Toluca 50200, Mexico; arvilchisn@uaemex.mx
* Correspondence: alien.blanco@test.edu.mx (A.B.F.); dreyesc@uaemex.mx (D.R.C.)

Abstract

This work presents a sustainable strategy for the fabrication of multifunctional silver nanoparticles (Ag-NPs) and Ag/jute nanocomposites using *Erythroxylum coca* tea waste extract as a bioreducing and stabilizing agent, combined with picosecond pulsed laser irradiation. UV–Vis spectroscopy and transmission electron microscopy revealed the formation of Ag-NPs with diverse morphologies and broad size distributions, which became significantly more uniform after laser post-treatment without the need for additional chemical reagents. Following laser irradiation, the initially broad Ag surface plasmon resonance (SPR) peak transformed into a symmetric Gaussian-shaped band, centered at 407 ± 3 nm for all the Ag-NPs systems. The catalytic performance of unsupported Ag-NPs and Ag-NPs supported on jute fibers was comparatively evaluated by degrading Congo red (CR) dye, revealing that the supported nanocomposites exhibited enhanced catalytic stability, higher pollutant removal efficiency, and improved catalyst recovery. Furthermore, multicomponent catalytic reduction experiments involving CR and 4-nitrophenol (4-NP) in the presence of $NaBH_4$ revealed simultaneous degradation and reduction pathways mediated by the Ag/jute nanocomposites, as evidenced by the emergence of new absorption bands during the reaction. In parallel, the synthesized Ag-NPs demonstrated pronounced antimicrobial activity against *Escherichia coli*, generating well-defined inhibition zones. Beyond conventional approaches centered on nanoparticle synthesis and morphology optimization, this study establishes a platform that combines agricultural waste valorization, laser-assisted nanoparticle engineering, and natural-fiber-supported nanocomposite fabrication, enabling efficient remediation of both single- and multicomponent pollutant systems while promoting catalyst reusability and environmental sustainability. These findings demonstrate the

Check for updates

Academic Editor: Jeevithan Elango

Received: 22 May 2026
Revised: 19 June 2026
Accepted: 23 June 2026
Published: 28 June 2026

Copyright: © 2026 by the authors. Licensee MDPI, Basel, Switzerland. This article is an open access article distributed under the terms and conditions of the Creative Commons Attribution (CC BY) license.

Ag/jute nanocomposites as sustainable and scalable catalytic materials for wastewater remediation and antimicrobial applications.

Keywords: *Erythroxylum coca* tea waste; pulsed laser irradiation; multicomponent pollutant remediation; Ag/jute nanocomposites; biosynthesis of silver nanoparticles; antimicrobial activity

1. Introduction

Silver nanoparticles (Ag-NPs) have been extensively studied, and several methods have been created, modified, or fused to understand and predict their optical and structural properties. Since the Turkevich method adaptation, originally using citrate reduction of metal salts to obtain gold nanoparticles, and later adapted for Ag-NP synthesis [1], routes of synthesis using different solvents [2,3], physical methods [4], or recent biological methods [5,6] all represent a move toward more controlled production approaches in colloid science. Even with the extensive reports on the synthesis of silver nanoparticles, these methods remain highly relevant due to their broad range of applications in medicine, industry, and environmental science [7,8]. Ag-NPs exhibit antimicrobial properties, making them strong candidates for applications such as antibacterial coatings [9], wound dressings [10], and sterilization agents [11]. Their distinctive optical features, most notably surface plasmon resonance, are also crucial for biosensing and diagnostic technologies [12]. Beyond biomedical applications, Ag-NPs also play an important role in catalysis and environmental remediation, including water purification systems [13,14]. In response to the growing demand for sustainable materials, green synthesis approaches using biological routes, such as plant extracts or microorganisms, have gained increasing attention. These methods offer an eco-friendlier and less toxic alternative for Ag-NPs production [15].

The advantages of biosynthesis include reduced environmental toxicity and the use of non-polluting substances [16]. Plant extracts are especially promising for nanoparticle biosynthesis, providing a broad spectrum of bioactive compounds that serve as reducing and stabilizing agents during synthesis. Compared to bacteria- and fungi-based methods, plant extracts not only minimize contamination risks in the final product but also enable faster and simpler production of high-purity nanoparticles [17–20]. In the biosynthesis process using plant extracts, nanoparticle size and morphology are influenced by the composition of the internal metabolites. These metabolites act as reducing and stabilizing agents, thereby influencing the reduction and stabilization of metal ions, resulting in nanoparticles with specific characteristics (such as size, shape, and distribution) that are highly dependent on the compounds in the extract used [21,22]. Since nanoparticle size and shape define their applications, precise control over these parameters is essential.

Authors such as Liu et al. [23] report the generation of spherical nanoparticles (NPs) of controlled sizes through laser irradiation. Parameters such as irradiation time, wavelength, laser fluence, pulse duration, and aqueous medium allow for precise control over NP morphology. Additionally, laser irradiation has been shown to induce morphological changes in NPs, commonly resulting in fragmentation and fusion at moderate radiation intensities. This results in spherical NPs of varying sizes, but in an acetone-water solvent, the irradiation spontaneously yields cubic morphologies. This is inferred to arise from a process analogous to chemical reduction, wherein silver atoms move between Ag-NPs [24]. The laser irradiation method is simple and avoids the use of chemical reagents that produce toxic by-products. It enables controlled NP formation by adjusting irradiation parameters

and the liquid medium [25]. The irradiated NPs exhibit specific properties that significantly impact their optical, electronic, magnetic, and antimicrobial applications [24].

The *Erythroxylum coca* leaf, native to the Andean region of South America, is traditionally consumed as coca tea, particularly in Bolivia and Peru, where it is known for alleviating altitude sickness, boosting energy, and aiding digestion. This plant is a matrix rich in alkaloids and various metabolites that are considered potent reducing agents [26], making it a suitable candidate for the biosynthesis of metal nanoparticles. Using this plant to obtain nanoparticles avoids adding synthetic surfactants, which also negatively impact the environment. After brewing, the tea bags are typically discarded as waste, although the organic solid residue still retains various bioactive metabolites, such as alkaloids and flavonoids, which can effectively reduce silver ions and stabilize nanoparticles. In general terms, several recent reviews indicate that approximately 5 million tons of tea waste are generated worldwide annually after consumption, much of which ends up in landfills or is used to a limited extent [27]. One potential application is the green synthesis of nanoparticles, which uses polyphenols and other metabolites found in a wide variety of teas [28]. This idea is one of the most recent lines of research to report the greatest technological potential. Therefore, the use of tea waste for the biosynthesis of metal nanoparticles not only reduces organic waste generation but also transforms an abundant, low-cost byproduct into functional materials with environmental and antimicrobial applications, contributing to the principles of the circular economy and green chemistry. It should be noted that, in the specific case of this study, although the coca leaf has been extensively studied for its alkaloids, its residual biomass also constitutes a rich source of phenolic compounds and antioxidants that can be utilized in green synthesis processes. However, studies aimed at valorizing coca infusion residues for the production of functional nanomaterials remain scarce. In the case of coca tea, once consumed, the solid residue is also considered a byproduct, making it a valuable and unconventional resource for reuse. From a scientific perspective, coca represents an innovative strategy for the technological revaluation of an underutilized plant, focusing on its use for obtaining nanomaterials with potential applications as antimicrobials and catalysts. From a scientific perspective, coca represents an innovative strategy for the technological revaluation of an underutilized plant, shifting the focus to its use in producing nanomaterials with potential applications as antimicrobials and catalysts.

Despite the large number of published articles on silver nanoparticles obtained from natural extracts for the catalytic removal of organic pollutants [29–31], they mainly focus on (i) free Ag-NPs in solution and (ii) tests with a single pollutant, the latter limiting extrapolation to real-world effluents. In this regard, information that simultaneously integrates a high-value phytochemical reducing agent such as *Erythroxylum coca* leaf extract, the immobilization of Ag-NPs on a renewable lignocellulosic support like jute fiber (because this facilitates recovery and minimizes nanoparticle release), and the evaluation under a multicomponent system (azo dye Congo Red and 4-nitrophenol) is particularly scarce. Organic compounds are common pollutants and exhibit diverse competitive interactions.

While it is true that reports of biosynthesis using lasers have been found, these studies describe the use of laser irradiation to synthesize metal nanoparticles in the presence of surfactants such as SDS and CTAB, which help coat and stabilize the nanoparticles [32,33], but there have been no reports of the combined use of natural extracts and laser application to improve the morphology of silver nanoparticles.

The literature reports that one of the most significant environmental problems is the contamination of surface water sources by dyes and pesticides, due to their high toxicity, persistence, and resistance to conventional treatment methods. Notable examples of these pollutants include Congo red and 4-nitrophenol, both of which are characterized by their

widespread industrial use and significant negative impact on aquatic ecosystems and human health. Although many studies have reported on the use of various materials for environmental remediation, including catalytic processes, these studies focus on single-component removal—a far cry from real-world effluents, which contain a mixture of contaminants. Therefore, multicomponent studies are essential for developing materials with greater applicability in environmental decontamination [34]. This is precisely part of the novelty and significance of the research being presented.

While it is true that Ag-NPs have demonstrated high catalytic efficiency and antimicrobial activity, when in the free state, they exhibit limitations associated with aggregation, low stability, and difficulty in recovery after the intended process (adsorption, catalysis, etc.). As an alternative, the immobilization of nanoparticles on natural lignocellulosic support [35] is a potential approach to improve their stability, reusability, and handling [36]. Among these supports, jute fiber stands out for its low cost, biodegradability, and abundance of surface functional groups favorable for nanoparticle anchoring. It is worth noting that anchoring silver nanoparticles to jute fibers represents a promising and innovative approach for applications such as textile filters, removable membranes, or reactive barriers, which are useful in continuous or modular water treatment systems, enabling easy material recovery and reducing the risk of nanoparticle release.

Despite advances in the green synthesis of Ag nanoparticles, few studies integrate the use of plant waste, post-synthesis modification via laser irradiation, and the fabrication of nanocomposites supported by natural fibers for applications in single- and multi-component catalytic degradation. For this reason, the results presented in this manuscript are considered relevant for applications in the environmental field and for antimicrobial properties.

Therefore, the present study introduces a novel design for a "green-recoverable" multifunctional hybrid material and evaluates it under conditions that more closely represent complex matrices, thereby generating important evidence on the relative contributions of adsorption and catalytic degradation in the presence of two competitive contaminants.

Antibiotic resistance among Enterobacterales is a major clinical challenge, especially among extraintestinal pathogenic *Escherichia coli* (ExPEC), which frequently carries virulence traits and extended-spectrum β-lactamases and is associated with hard-to-treat infections [37]. Within ExPEC, uropathogenic *E. coli* (UPEC) is particularly relevant because it combines antimicrobial resistance with strong colonization capacity and frequent biofilm formation, contributing to persistence and recurrence [38,39].

In this context, various studies have demonstrated that silver nanoparticles exhibit significant antibacterial activity against a broad spectrum of pathogenic microorganisms, including both Gram-positive and Gram-negative bacteria, through multi-target effects such as membrane damage, localized oxidative stress, and the release of silver species [40,41]. Moreover, Ag-NPs have been investigated as anti-biofilm materials, showing potential to inhibit biofilm formation and disrupt established biofilms; however, their performance is strongly influenced by physicochemical parameters such as particle size, surface chemistry, and colloidal stability [42–44]. Spherical Ag-NPs have been widely reported as potent antimicrobial [38,45].

In this study, we report the green synthesis of Ag-NPs using an extract from *Erythroxylum coca* leaves, followed by controlled pulsed-laser irradiation to refine the nanoparticle morphology. The incorporation of pulsed laser processing enables more precise regulation of nanoparticle size and shape, thereby enhancing their suitability for various technological and biomedical applications. This hybrid strategy, which integrates an active plant-derived waste product, not only improves the physicochemical properties of the resulting nanoparticles but also contributes to cleaner and more sustainable materials production. The

as-synthesized Ag-NPs were further evaluated for their catalytic and adsorptive performance by degrading Congo Red dye, using a multi-component system to assess their environmental viability. Results show the multifunctionality of the Ag-NPs, including dye degradation, antimicrobial for *E. coli* strains, and the immobilization on a complex matrix (jute fiber).

From an industrial perspective, the potential benefits and applications at this large scale go beyond simply enhancing the catalytic and antibacterial activity of the system under analysis. The use of a lignocellulosic support, such as jute, prevents the nanoparticles from dispersing in aquatic environments, which would make their recovery difficult; it could also lead to undesirable effects in living organisms due to the presence of very small particles. In addition, it facilitates the recovery and reuse of the material after treatment and promotes its implementation in pilot- or industrial-scale water treatment systems.

2. Materials and Methods

2.1. Materials

The materials used in this study are as follows: deionized water, silver nitrate ($AgNO_3$) from Fermont, sodium borohydride ($NaBH_4$), Congo Red dye ($C_{32}H_{22}N_6Na_2O_6S_2$), 4-nitrophenol ($C_6H_5NO_4$) from Sigma-Aldrich, as well as Agar from Mueller-Hinton Agar, and LB Broth Miller from Criterion Dehydrated Culture Media.

2.2. Biosynthesis Method

The research presented here does not treat biosynthesis as a method independent of laser pulsing, but rather as two complementary methods. The combination of biosynthesis mediated by residual *Erythroxylum coca* tea extract and picosecond-pulsed laser irradiation constitutes a hybrid strategy that integrates the benefits of green chemistry and the valorization of biological waste with precise control over the physicochemical properties of nanoparticles. In this way, nanomaterials with optimized structural characteristics can be obtained for applications in the treatment of water contaminated with organic compounds and microbiological presence that must be controlled, where catalytic activity, stability, and surface interaction play a decisive role in the functional performance of the resulting material [46,47].

2.2.1. Preparation of *Erythroxylum coca* Tea Extract

The extract was prepared as follows: Erythroxylum coca leaf powder was obtained from a commercial tea by Windsor. After brewing the tea, the contents of the bag were collected, dried at room temperature, and ground into a fine powder using a mortar and pestle. In a 50 mL beaker, 20 mL of deionized water was heated to 60 °C. Subsequently, 0.2 g of *Erythroxylum coca* leaf powder was added, and the mixture was maintained for 7 min. Finally, the extract was filtered and stored for later use.

2.2.2. Biosynthesis of Silver Nanoparticles

The biosynthesis was carried out by adjusting the experimental conditions of the experiments reported by Morales-Luckie et al. [48]. The authors demonstrated that jute fibers functionalized with biosynthesized AgNPs exhibited antifungal activity, which is why we are using it as a starting point for our research.

The effect of extract dilution on the biosynthesis process was investigated by using three different biosynthesis systems containing varying amounts of extract: pure extract, a 1:10 dilution (pure extract and deionized water), and a 1:20 dilution. These dilutions of the pure extract were used to simulate the conditions of the aqueous residue obtained after preparing and consuming infusions, i.e., the state of the tea after ingestion. A 5 mL

aliquot of a 0.001 M silver ion precursor solution was placed in a vial, and then 2 mL of *Erythroxylum coca* extract was added dropwise. Finally, the mixture was brought to a total volume of 20 mL by adding deionized water and stirred for 1 min to ensure homogeneity. The reaction was monitored by observing color changes and by UV-Vis spectroscopy (Velaquin, Mexico City, Mexico) to track the Surface Plasmon Resonance (SPR) peak.

2.2.3. Laser Irradiation of Biosynthesized Ag-NPs

Following the strategy demonstrated by Carpio-Martínez et al. [49], laser irradiation after biosynthesis is an effective tool for modulating the size and morphology of noble metal nanoparticles. The combination of plant extracts as reducing and stabilizing agents with physical laser treatment allows for the production of sustainable nanomaterials whose surface properties can be optimized for catalytic and antimicrobial applications. Although the authors did not use the same extract, their work serves as a starting point for demonstrating that laser irradiation can precisely tune the functional properties of nanoparticles. In this research, another hypothesis is tested using a different type of plant extract.

In a vial, 10 mL of the colloidal Ag-NPs obtained by the biosynthesis method were irradiated with a picosecond pulsed Nd laser (Ekspla, Vilnius, Lithuania) at 1064 nm, pulse energy of 30 mJ, and repetition rate of 10 Hz. This process was conducted in 5 min intervals. These will henceforth be referred to as AgNP-L. The NPs plasmon peak was identified after each irradiation by UV-Vis spectroscopy.

2.2.4. Characterization of Ag-NPs

The biosynthesized and irradiated nanoparticles (Ag-NPs and AgNP-L, respectively) were characterized using UV-Vis spectroscopy with a VELAB brand instrument. The morphology and size of these were analyzed using Transmission Electron Microscopy (TEM), JEOL-2100, JEOL USA, Inc., Peabody, MA, USA.

2.3. Degradation of Congo Red and Congo Red/4-Nitrophenol Systems and Antimicrobial Evaluation

2.3.1. Incorporation of the Ag-NPs into Jute Fiber

The influence of support on pollutant removal/degradation was studied. Jute fiber, a natural biopolymer abundant in Mexico and widely used in the textile industry, was selected as the support. The nanoparticles were supported on this biopolymer, and the process was studied in the presence and absence of sodium borohydride. The results were compared only with those obtained for non-irradiated silver nanoparticles, considering the presence and absence of this reducing agent. The amounts of $NaBH_4$ and the concentration of Congo Red were the same as in previous experiments. AgNP–Jute fibers (Ag/jute nanocomposites) used per volume of dye was 0.1 g. To analyze the efficiency of the nanoparticles supported on the fibers, the multicomponent adsorption/degradation of Congo Red and 4-nitrophenol was also studied.

2.3.2. Degradation of Congo Red Dye

The adsorption/degradation experiment involved adding 50 mL of a Congo red dye solution (1.3×10^{-3} M) to a 100-mL beaker. Subsequently, 2 mL of colloidal solutions of synthesized non-irradiated and irradiated nanoparticles (Ag-NPs and AgNP-L, respectively) was introduced. The mixture was stirred at 250 rpm for 1 min to achieve homogeneity. Following this, 3 mL of a 5×10^{-4} M sodium borohydride solution was added, with constant agitation throughout the experiment. The kinetics of the degradation process were monitored using UV-Vis spectroscopy at various time intervals (0, 3, 6, 9, 12, 15, 30, 45, 60, 90, 120, 150, 180, and 210 min), and the corresponding absorption spectrum for each sampled aliquot was recorded.

The multicomponent adsorption/degradation of Congo Red and 4-nitrophenol (4NP) was also studied. In a beaker, 50 mL of Congo Red dye solution (initial concentration 1.3×10^{-3} M), 5 mL of 4-nitrophenol solution (2×10^{-3} M), and 0.5 g of jute fiber coated with silver nanoparticles were mixed. Subsequently, 8 mL of sodium borohydride solution (5×10^{-3} M) was added. The system was kept in constant agitation, and samples were taken at intervals of 3 min to 210 min. Quantification was performed by obtaining absorption spectra and identifying the peaks of each contaminant at different wavelengths.

2.3.3. Assessment of Antimicrobial Activity

Microbiological tests were performed using three colloidal nanoparticle systems: Ag-NPs biosynthesized with pure coca extract and with 1:10 and 1:20 dilutions of the extract (Ag-NPs (1:10) and Ag-NPs (1:20)). Both irradiated and non-irradiated nanoparticle suspensions were tested.

Five strongly biofilm-forming Enterobacterales clinical isolates were used: AME 16, ARH 1, CCI 11, FMD 1, and HHM 25, along with a reference/control strain, *E. coli* ATCC 25922. The strains were selected based on a biofilm screening protocol and characterized by antibiotic susceptibility testing following EUCAST [50] breakpoint tables (version 12.0); all strains showed resistance to ampicillin (AMP) and most of them to cefotaxime (CTX), while *E. coli* ATCC 25922 showed an intermediate phenotype for AMP and susceptibility to CTX.

The antimicrobial activity of the Ag-NPs was first evaluated by soft-agar overlay assay described by Hockett & Baltrus [51], as this format is suitable for liquid/colloidal samples.

For the overlay assay, bacteria were grown overnight in LB broth, diluted 1:100, and incubated for an additional 4 h in Mueller-Hinton broth. Then, 100 µL of the culture was mixed with 3 mL of warm sterile 0.5% agar and spread onto Mueller–Hinton agar plates. After 5 min, 5 µL of each Ag-NPs suspension and its control ($AgNO_3$) were dispensed into the marked positions on the plates and incubated at 37 °C for 24 h. Inhibition zones were quantified as area (mm^2) using ImageJ v1.53t [52]. For each strain, three independent assays were performed, each including three technical replicates.

Biofilm inhibition was assessed by a microtiter-plate crystal violet assay following Barabadi et al. [53]. Briefly, cultures were grown for 3 h in TSB, adjusted to 0.5 McFarland (OD600), diluted 1:100, and dispensed into 96-well plates (final volume: 200 µL) containing AgNPs at concentrations corresponding to 0.5×, 1×, 1.5×, and 2× MIC (MIC values determined by broth microdilution as described by Wiegand et al. [54]. Plates were incubated at 37 °C for 24 h. Wells were washed three times with sterile deionized water, fixed with 200 µL of 95% ethanol, stained with 0.1% crystal violet for 15 min, washed again (3×), air-dried (30 min), and the dye was solubilized with 250 µL of 33% glacial acetic acid. Absorbance was read at 570 nm, and biofilm inhibition (%) was calculated relative to the growth control. Each condition was tested in triplicate wells, including growth, sterility, extract, water, and $AgNO_3$ controls.

3. Results and Discussion

3.1. Biosynthesized Ag-NPs

Erythroxylum coca extract has been shown to contain various bioactive compounds, including alkaloids, flavonoids, phenols, and carbohydrates [55,56]. Flavonoids, which feature diverse functional groups, play a key role in reducing metal ions, facilitating nanoparticle synthesis [57]. Additionally, the phenolic compounds in the extract act as ligands, serving primarily as stabilizers that inhibit nanoparticle growth and prevent aggregation [58]. Upon mixing *Erythroxylum coca* extract with a silver ion solution, the initially clear solution turns brown, with the intensity of the coloration depending on both the extract concentration and the time elapsed after synthesis. This color change visually

indicates the formation of nanoparticles, as illustrated in Figure 1a, which shows real-time images of Ag-NPs as they form.

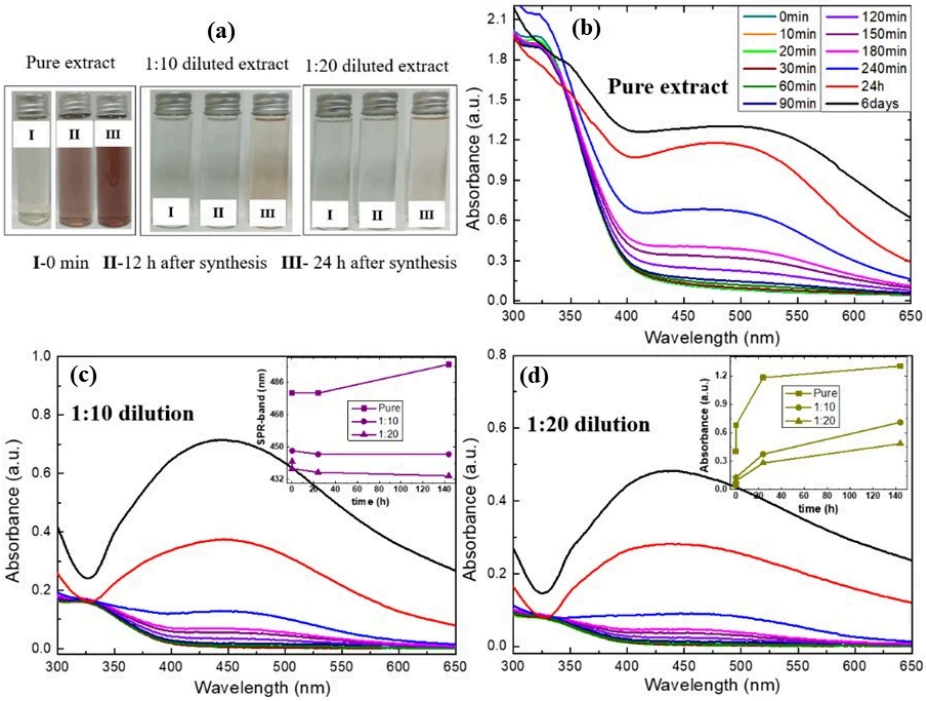


Figure 1. (**a**) Actual pictures of the Ag-NPs solutions under the different dilutions and times after its synthesis. Absorbance spectrum of the nanoparticle solution synthesized with (**b**) pure extract, (**c**) 1:10 diluted extract (inset is the SPR position for three selected times), and (**d**), 1:20 diluted extract (inset is the absorbance intensity for three selected times).

The influence of extract concentration on the biosynthesis of Ag-NPs was evaluated by monitoring the time-dependent evolution of their absorbance spectra. Figure 1b–d correspond to the undiluted extract, 1:10 dilution, and 1:20 dilution, respectively. In all cases, the SPR band serves as an indicator of Ag-NPs formation. For the pure extract, a well-defined SPR band emerged after 120 min (pink line), whereas for both the 1:10 and 1:20 dilutions, the SPR feature appeared later, at 240 min (blue lines). At these characteristic times, the SPR peak for the pure extract was located at 480 nm (Figure 1b), while the 1:10 and 1:20 dilutions exhibited blue-shifted peaks at approximately 446 nm and 434 nm, Figure 1c,d, respectively, though with less well-defined band shapes.

As the reaction time increased, absorbance rose progressively, consistent with the continuous formation of Ag-NPs. After approximately 144 h (6 days), the SPR band of the sample synthesized with the pure extract exhibited a light red-shift to 497 nm, whereas the SPR peaks of the diluted-extract samples remained nearly constant at 448 nm and 442 nm. This behavior is illustrated in the insets of Figure 1c,d.

In Figure 1c,d, the SPR bands appear well-defined and comparatively narrow, indicating that the nanoparticles formed in the diluted systems are more size-uniform in smaller quantities. The decrease in extract concentration resulted in a noticeable reduction in SPR intensity at longer times, reflecting a slower Ag-NPs formation rate. This is clearly evidenced in the inset of Figure 1d. The 1:20 dilution exhibited the lowest degree of nanoparticle formation, likely due to its reduced concentration of bio-reductive phytochemicals [59] (Figure 1d).

In the graphs shown in Figure 1b–d, the increasing absorbance values are associated with greater Ag-NPs formation until day six, when maximum formation was achieved. Over time, the concentration of colloidal nanoparticles increased, and it is precisely at

minute 240 that their characteristic peak is clearly observed. No plasmon shift occurs during the synthesis period; this precisely suggests that the morphology and size remained constant. As the absorbance values increased progressively during this time period, this is interpreted as continuous nanoparticle formation due to the gradual reduction of silver ions by the bioreducing agents present in the coca leaf tea residue extract. Iravani reportó que la síntesis utilizando extractos vegetales implica que la reducción puede ocurrir de forma gradual por la acción de múltiples bioreductores presentes en los extractos vegetales [60]. This allows us to infer that the reduction kinetics are slow but with controlled growth.

To confirm this approach, the pseudo-first-order model [61] and the Avrami model [62] were applied. The former was used to determine the value of the rate constant for nanoparticle formation. The latter was used to determine the value of the model's constant "n," which helps interpret whether continuous nucleation and controlled growth are occurring. The results are shown in Table 1.

Table 1. Parameters of the kinetic models used to study the formation of Ag-nanoparticles.

Pseudo First Order (p − 1) Model			
Synthesized Systems	**k_{p-1} (min^{-1})**		**R^2**
Ag-NPs $_{\text{pure extract}}$	0.00153		0.9683
$Ag\text{-}NPs_{1:10}$	5.124×10^{-5}		0.9872
$Ag\text{-}NPs_{1:20}$	0.00154		0.9754
Avrami Model			
Synthesized systems	k_A (min^{-1})	n	R^2
Ag-NPs $_{\text{pure extract}}$	$2.737 \cdot 10^{-4}$	1.2896	0.8689
$Ag\text{-}NPs_{1:10}$	$6.818 \cdot 10^{-5}$	1.3297	0.8792
$Ag\text{-}NPs_{1:20}$	$1.060 \cdot 10^{-3}$	1.0178	0.8983

Given the low rate constants for both models ($k_{p\text{-}1}$ and k_A), the nanoparticle formation process is indeed slow. The values of "n" fall within the range of 1 and 2 ($1 \leq n < 2$), indicating that a process of continuous nucleation with restricted growth is taking place. This is consistent with the absence of a shift in the characteristic SPR band, as observed in Figure 1b–d. This indicates that the increase in absorbance is indeed due to the progressive formation of new particles, rather than the growth of already formed particles.

3.2. Irradiated Ag-NPs

Upon irradiation of the synthesized nanoparticles, for the new AgNP-L suspensions, one of the most evident indicators of laser-induced modification is the change in the color of the colloidal solution (inset in Figure 2a–c). The characteristic brown coloration of the AgNP-L dispersion (labeled "2" in the insets) becomes noticeably lighter after laser exposure (labeled "1"), suggesting alterations in the optical properties of the system. These changes are likely due to the photodegradation of organic molecules in the extract, as many phytochemical species undergo bond cleavage under laser irradiation, generating smaller or structurally modified photoproducts [63]. Such photoproducts often exhibit absorption features distinct from those of the native compounds, thereby modifying the overall color and optical response of the AgNP-L suspension.

In Figure 2a, the SPR absorption band of the unirradiated sample synthesized with pure extract is centered at 525 nm and appears broad, poorly defined, and asymmetric (black line). Such broadening is typically associated with a wide size distribution and morphological heterogeneity in Ag-NPs, as larger or irregularly shaped particles experience

greater damping, broadening the plasmon band [64]. After 5 and 10 min of pulsed laser irradiation, the SPR band undergoes a noticeable blue shift and becomes significantly more symmetric and narrower, indicating a transition toward a more uniform nanoparticle population. This behavior suggests that pulsed laser irradiation induces fragmentation of larger nanoparticles into smaller ones, i.e., more uniformly sized Ag-NPs. A similar trend is observed for the biosynthesized irradiated nanoparticles using diluted extracts (Figure 2b,c). The observed SPR blue-shift and band narrowing are consistent with changes in nanoparticle morphology, specifically the formation of smaller, more spherical particles, as previously reported for biogenic Ag and Au nanoparticles irradiated during synthesis with *Citrus paradisi* extracts [65].

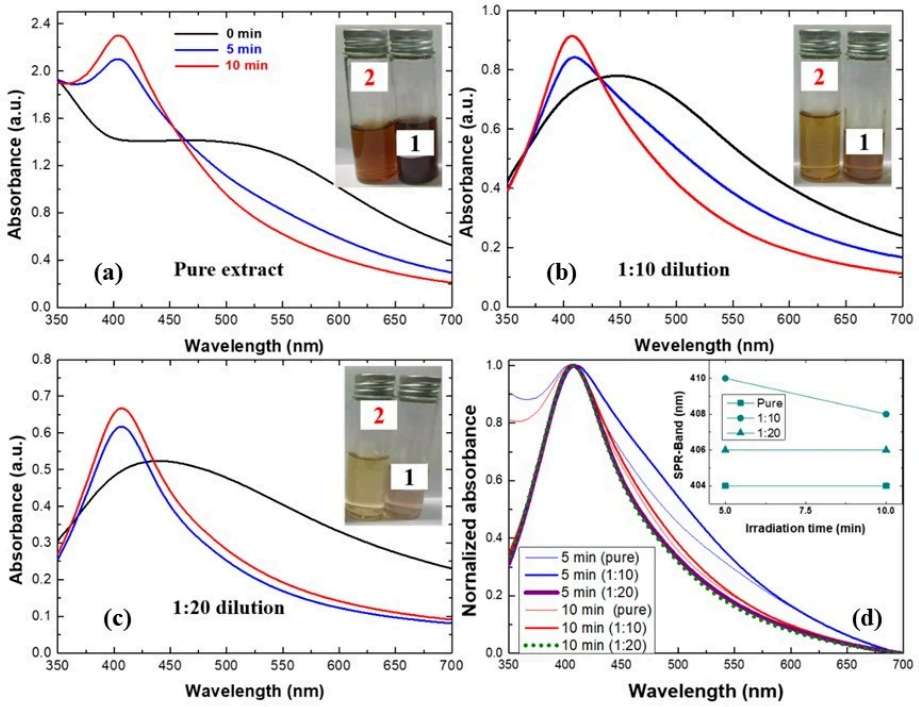


Figure 2. Absorbance spectrum of the Ag-NPs-L solutions before and after the laser irradiation by 5 and 10 min. (**a**) pure extract, (**b**) 1:10 dilution, and (**c**) 1:20 dilutions insets correspond to the unirradiated (1) and irradiated (2) solutions. (**d**) Normalized absorbance of the irradiated solutions for comparison (inset is the SPR position for 5 and 10 min of irradiation times).

In Figure 2a, the SPR band of the non-irradiated Ag-NPs biosynthesized with pure extract is at 480 nm. After 5 and 10 min of pulsed laser irradiation, this peak blue-shifts to 404 nm, accompanied by a slight increase in absorbance for the 10 min exposure and a pronounced narrowing of the band. This behavior indicates that laser irradiation induces significant size modification, generating a higher population of smaller Ag-NPs whose plasmon response is near 405 nm. The normalized spectra in Figure 2d (thin lines) further reveal subtle changes in the overall band shape, particularly in the spectral regions outside the SPR maximum, suggesting variations in nanoparticle morphology and polydispersity.

A similar trend is observed for the samples synthesized from diluted extracts. For the 1:10 dilution (Figure 2b), the SPR peak shifts from 448 nm in the non-irradiated sample to 410 nm and 408 nm after 5 and 10 min of irradiation, respectively. In the most diluted sample (1:20), the SPR maximum shifts from 442 nm to 406 nm for both irradiation times. These consistent blue shifts across all extract concentrations confirm that laser irradiation promotes the formation of smaller, more uniformly distributed nanoparticles.

The SPR shifts for all three samples at both irradiation times are summarized in the inset of Figure 2d, which shows that, regardless of the biosynthesis conditions or irradiation

duration, the SPR band is centered within a very narrow 404–408 nm (4 nm interval), with an average value of 406 nm. Notably, for the 1:20 dilution (bold purple and green dashed lines), the SPR band after irradiation becomes highly symmetric and maintains a consistent shape, in contrast to the broad, asymmetric band observed before laser exposure. This symmetry suggests greater uniformity in nanoparticle morphology, indicating a larger population of spherical AgNP-L. Such uniformity likely results from the reduced extract concentration, which minimizes the presence of photodegradable organic molecules that could otherwise interfere with nanoparticle reshaping during laser irradiation.

The full width at half maximum (FWHM) for the recorded and normalized absorbance spectra for the irradiated samples was determined to be 100 nm in both cases; only 5 min of irradiation is sufficient to achieve a well-defined SPR band. Similar behavior has been reported for biosynthesized Ag-NPs using *Citrus paradisi* extracts, where the SPR peak stabilized at 400 nm after 6 min of irradiation with the same laser source. These results confirm the reproducibility of SPR-band tuning via pulsed laser irradiation, independent of the extract employed in the biosynthesis process [59].

It has been reported that Ag-NPs with predominantly spherical morphology exhibit a narrower SPR band, typically within the 400–450 nm range, due to uniform oscillation of surface electrons, which is strongly size-dependent. In contrast, broadening of the SPR band can indicate morphological heterogeneity, such as aggregation or non-spherical shapes, resulting in increased scattering [66]. The observed SPR features of the biosynthesized Ag-NPs therefore suggest that irradiation produces a predominantly spherical morphology with a uniform size distribution, as the recorded spectra exhibit near-symmetric, Gaussian-like SPR bands.

3.3. Morphological Characterization of the Unirradiated and Irradiated Ag-NPs

Two extreme synthesis conditions were selected for detailed evaluation: (i) Ag-NPs biosynthesized using the pure extract and its 1:20 dilution, and (ii) each of these samples in non-irradiated and laser-irradiated forms. These samples were characterized to elucidate the effects of extract concentration and laser irradiation on their structural features, as the optical properties were significantly modified.

Morphological analysis via Transmission Electron Microscopy (TEM and HRTEM) provided detailed insights into the shape, size, and crystal structure of the synthesized Ag-NPs. In all cases, the nanoparticles exhibited a predominantly quasi-spherical morphology, with variations in sphericity and size depending on the synthesis conditions (Figure 3a–i). In general, the sizes obtained from all syntheses are lower than those reported in the literature. For example, Eker et al. [67] reported several green syntheses of AgNPs using different plant extracts, and they emphasized the influence of phytochemicals on nanoparticle formation and size, among other important parameters. The authors demonstrated that, using this method, the size can vary, with nanoparticles ranging from 15 to 180 nm, exceeding the values obtained in our research. The same results were obtained by Fahim et al. [15]. Also, Syed et al. reported in their research that green methods using plant extracts, the typical size of nanoparticles, such as Au nanoparticles, is between 10 and 50 nm [68].

In our case, the extract used is rich in alkaloids. It can be hypothesized that the small particle sizes obtained—regardless of whether the sample was irradiated or not—may be due to the fact that the alkaloids, on the one hand, reduce silver ions and adsorb onto the surface, thereby inhibiting the growth of the nanoparticles. Alternatively, since the alkaloids contain nitrogen groups, these coordinate with ions to form complexes that slow reduction and control nucleation [69].

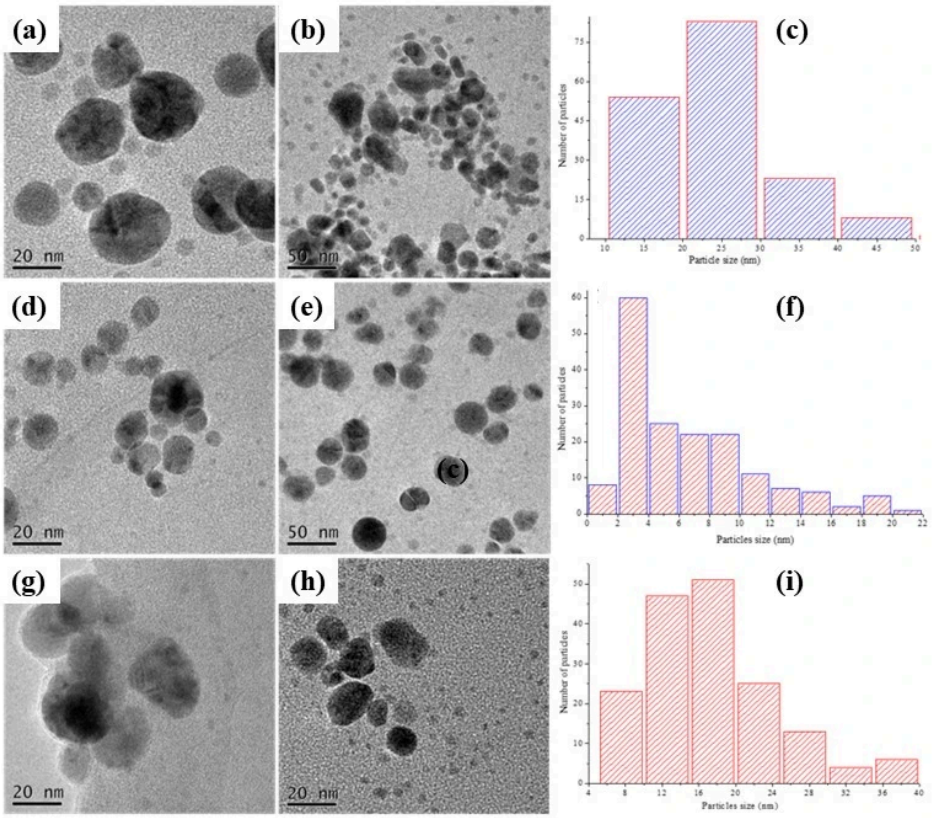


Figure 3. TEM micrographs of Ag-NPs synthesized with pure, unirradiated extract (**a**,**b**), with pure, irradiated extract (**d**,**e**), and with 1:20 dilution of the extract and irradiated (**g**,**h**), and histograms for these ((**c**), (**f**), and (**i**), respectively).

For nanoparticles synthesized with the pure extract without irradiation, the average size was 25 nm, with significant polydispersity and shapes varying from quasi-spherical to ellipsoidal (Figure 3a–c).

In contrast, irradiation of nanoparticles synthesized with the pure extract resulted in a substantial size reduction to 2–4 nm, with a more uniform and nearly spherical morphology (Figure 3d,e). Interestingly, when nanoparticles were synthesized from the 1:20-diluted extract and subsequently irradiated, their size increased to 15–20 nm while maintaining a nearly spherical shape (Figure 3e). These results indicate that pulsed laser irradiation effectively fragments larger nanoparticles and promotes more uniform size and shape distributions, though the initial extract concentration influences the final particle dimensions. This behavior is due to the pure extract containing a higher concentration of bioreducers and stabilizing agents for the nanoparticles after synthesis. These compounds cause metallic silver nucleation to proceed rapidly and abundantly, thereby limiting the subsequent growth of metal nuclei as they become coated on the surface. In contrast to using a diluted extract for biosynthesis—in which the concentration of reducing and stabilizing agents is much lower, reducing nucleation density—greater particle growth is possible during irradiation, resulting in particle sizes larger than 15–20 nm. Figure 4 shows a diagram of this process.

To date, the results obtained have demonstrated that picosecond-pulsed laser irradiation is an effective strategy for modifying the morphology and size distribution of AgNPs synthesized from *Erythroxylum coca* tea waste extract. Analysis of the UV-Vis spectra, particle size histograms, and TEM images clearly shows a decrease in morphological heterogeneity and a trend toward more uniform nanoparticle populations following laser treatment. This behavior is consistent with that reported by Carpio-Martínez et al. [49], who

demonstrated that irradiation of biogenic silver and gold nanoparticles with an Nd:YAG laser (532 nm) induces fragmentation and surface reorganization associated with localized photothermal heating.

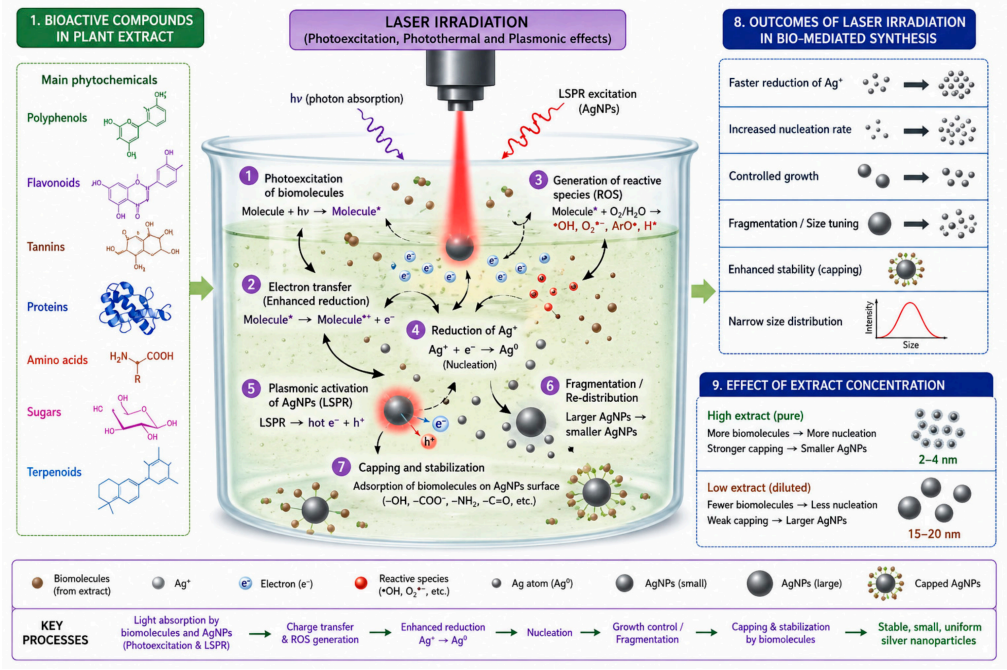


Figure 4. Effect of the irradiation process on nanoparticle size and the influence of extract concentration [70].

According to the authors, the absorption of laser energy via surface plasmon resonance generates a rapid transfer of energy to the crystal lattice, causing transient temperature increases high enough to induce partial melting, surface rounding, and fragmentation of larger particles. Consequently, the population of small nanoparticles increases, and the proportion of large or anisotropic particles decreases. For the research we present, the aforementioned mechanism provides a reasonable explanation for the morphological evolution observed in Ag-NPs obtained from *Erythroxylum coca*, in which laser post-treatment favored more homogeneous distributions without the need for additional chemical reagents. Carpio-Martínez et al. [49] report a nanoparticle size of 5 nm following laser treatment, whereas in our study, the size obtained after the same treatment was even smaller (2–4 nm), indicating that the extract obtained from *Erythroxylum coca* has a greater stabilizing capacity and that the chemical composition of this extract evidently influences the morphological response of the irradiated nanoparticles. Thus, the system formed by *Erythroxylum coca* extract and laser irradiation yields a smaller particle size than that reported by the authors for *Citrus paradisi* extract.

The interplanar distance measured from the HRTEM image of nanoparticles synthesized with the pure, non-irradiated extract was 2.21 Å (Figure 5a). This value corresponds to the (111) plane, possibly slightly distorted or inclined relative to the electron beam and is consistent with a metallic silver crystalline structure. Selected Area Electron Diffraction (SAED) analysis of the same sample (Figure 5b) confirmed a face-centered cubic (FCC) crystal structure. For nanoparticles synthesized with the pure extract and subsequently irradiated (Figure 5c) and for those synthesized with 1:20 diluted extract and irradiated (Figure 5f), the interplanar distances were measured as 2.35 Å and 2.08 Å, respectively, corresponding to the (111) and (200) planes of FCC Ag^0. The slight variations in these "d" values are attributed to particle size effects, lattice strain induced by laser irradiation, interactions with surface-adsorbed plant extract molecules, and potential defects or dif-

ferences in crystal orientation. These results confirm that, despite changes in size and morphology induced by synthesis conditions and laser treatment, all samples retain the metallic Ag phase.

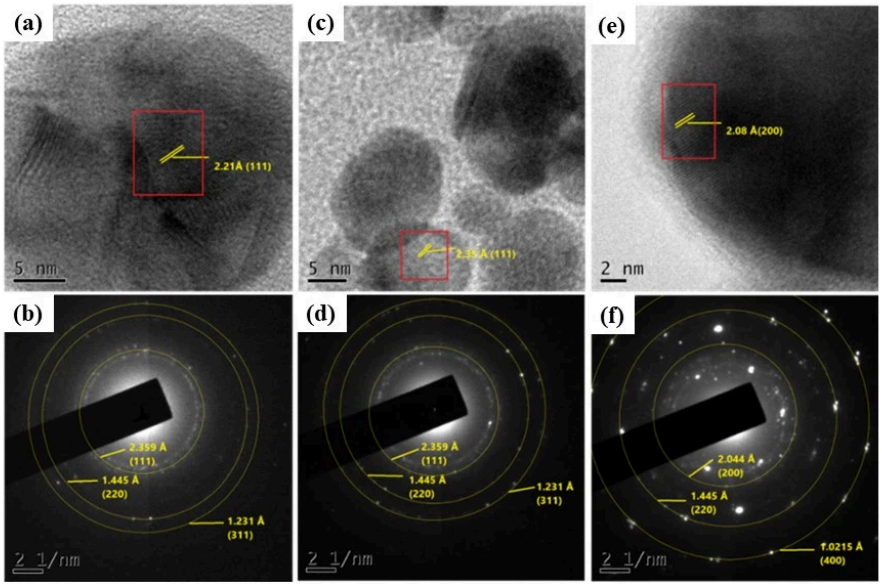


Figure 5. HRTEM images and SAED pattern of Ag-NPs biosynthesized with pure, unirradiated extract (**a**), with pure, irradiated extract (**c**), and with 1:20 dilution of the extract and irradiated (**e**), with their corresponding SAED characterization, (**b**), (**d**) and (**f**), respectively.

3.4. Degradation of Congo Red and Congo Red/4-Nitrophenol Systems and Antimicrobial Evaluation

3.4.1. Congo Red Dye Degradation Using Ag-NPs

To evaluate the effectiveness of non-irradiated and irradiated silver nanoparticles in removing CR dye, each system was analyzed under three conditions, considering the effect of adding $NaBH_4$. These were: (i) Interaction of CR with biosynthesized nanoparticles, comparing non-irradiated (Ag-NPs) and laser-irradiated (AgNP-L) systems without the addition of $NaBH_4$. The corresponding spectra versus time are shown in Figures 6a and 6b, respectively. (ii) Synergistic effect of $NaBH_4$ together with irradiated nanoparticles (AgNP-L+$NaBH_4$) and non-irradiated nanoparticles (AgNPs+$NaBH_4$), and (iii) Independent action of the reducing agent ($NaBH_4$) on CR without the addition of nanoparticles. The results are presented in Figures 6c, 6d and 6e, respectively. This experimental design allowed us to clearly distinguish the specific contribution of $NaBH_4$ and the differential roles of irradiated and non-irradiated Ag-NPs in the dye removal process.

In both unirradiated and irradiated cases, two characteristic absorption bands of CR dye were observed (Figure 6). The first, typically appearing between 488 and 500 nm [71], was recorded at 498 nm, which corresponds to the diazo chromophore (-N=N-). The second one was observed at 343 nm, associated with the p-π* transition of the aromatic ring (Figure 6f). The absorption spectra for each degradation condition were taken at different times, with 210 min being the largest.

As can be seen in Figure 6a,b, when the nanoparticles alone (unirradiated and irradiated) were added to the CR dye solution, the absorbance intensity of the bands at 498 nm and 343 nm increased, and after 180 min, a decrease of no more than 0.02 absorbance intensity was observed (Figure 6a, unirradiated system). This behavior is the same as that observed for the irradiated system, as shown in Figure 6b; however, both bands showed nearly the same absorbance after 180 min, indicating that the irradiated nanoparticles cannot reduce the CR dye. The authors report that this behavior may be due to three reasons:

when the laser struck the nanoparticles, their surface was passivated by the oxidation of the organic molecules coating them; a change in the surface electronic state (the nanoparticles may have oxidized and formed silver oxide); and a decrease in the number of electrons available for dye reduction, among other causes [72].

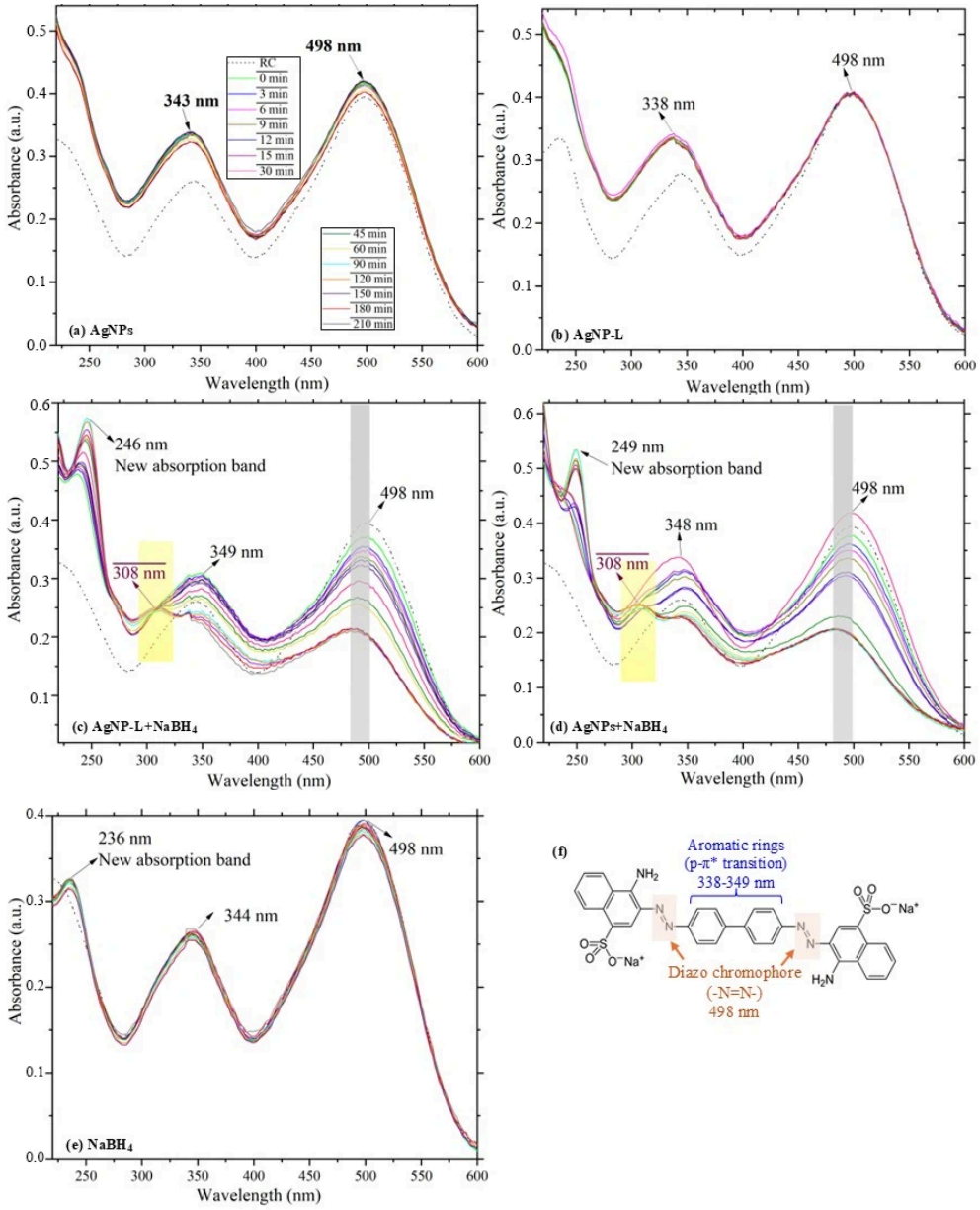


Figure 6. Consecutive absorbance spectra for the CR dye degradation exposed to (**a**) AgNPs, (**b**) AgNP-L, (**c**) AgNP-L+$NaBH_4$, (**d**) AgNPs+$NaBH_4$ combined system, (**e**) alone NaBH4 chemical compound, and (**f**) functional groups of CR associated with absorption bands.

$NaBH_4$ is a widely used reducing agent that reduces aldehydes, ketones, and some esters to their corresponding alcohols. As reported in Figure 6c,d, the combined system of nanoparticles irradiated and unirradiated, plus $NaBH_4$ (AgNP-L+$NaBH_4$ and AgNPs+$NaBH_4$) showed a substantial decrease in absorbance (0.2084 and 0.2056, respectively) values from the initial time point, indicating a strong synergistic effect between the nanoparticles and the sodium borohydride to promote the CR degradation. The literature reports that when nanoparticles are coated with agents containing nitrogen groups, they can exhibit greater catalytic activity [73], however, here the absorbance difference is 1.34%, showing similar CR degradation whether the sample is irradiated or not.

Notably, the peak associated with the diazo group (-N=N-) at 498 nm shifted to 484 nm between 45 and 120 min in both the unirradiated and irradiated systems (highlighted within the grey rectangle). This shift indicates chemical modifications in the dye structure during degradation, consistent with observations reported by Liu et al., [71]. Moreover, a new absorbance band emerged at lower wavelengths (246–248 nm) in both systems, suggesting partial fragmentation of the dye molecules and marking the onset of degradation. The catalytic activity of AgNPs is widely attributed to their electron-donating capacity, which promotes dye reduction in the presence of $NaBH_4$. The degradation process becomes significantly hindered when either component is absent, as both are required to establish the favorable redox and catalytic conditions necessary for efficient dye breakdown.

The band observed at 246–249 nm is attributed to $\pi \rightarrow \pi^*$ transitions characteristic of aromatic rings formed following the cleavage of the azo bond (–N=N–) in the dye. In addition to this feature, a second band appears at 308 nm (highlighted with the yellow rectangle) in both systems (AgNP-L+$NaBH_4$ and AgNPs+$NaBH_4$). This band corresponds to $n \rightarrow \pi^*$ transitions associated with amine and sulfonyl functional groups (–NH_2 and –SO_3^-), which emerge as intermediate products during CR degradation. The signal at 308 nm may also arise from charge-transfer interactions between the aromatic degradation products and the silver nanoparticle surface. Overall, these results suggest that CR degradation leads to the formation of simpler aromatic compounds, and that the dominant reaction pathway likely involves catalytic reduction of the azo groups, followed by fragmentation of the original chromophore.

To clarify the behavior observed under the combined condition, the effect of $NaBH_4$ alone was evaluated. Figure 6e shows the absorbance spectrum of the dye exposed solely to the reducing agent. As expected, the characteristic absorbance bands of CR remain essentially unchanged, indicating that $NaBH_4$ by itself does not alter the dye structure under these conditions. However, a band at 236 nm is observed, which is attributed to species derived from the reducing agent. Such features typically appear in the 230–250 nm range and are associated, for example, with $\sigma \rightarrow \sigma^*$ transitions of the B–H bond.

A proposed interaction mechanism promoting dye degradation is illustrated in Figure 7a. This mechanism is based on the formation of a σ-donor complex between borohydride ions and the metallic silver surface, leading to a metal–hydride intermediate. These intermediate releases electrons that are subsequently transferred to the dye molecules, triggering the reduction and cleavage of the azo groups. As a result, the chromophore structure is disrupted, producing smaller, less toxic molecules. It is also inferred that these degradation products may adsorb onto the nanoparticle surface through electrostatic interactions or via newly formed amine functional groups. Thus, the nanoparticles may act not only as catalytic platforms but also as efficient adsorbents for the by-products generated during dye degradation.

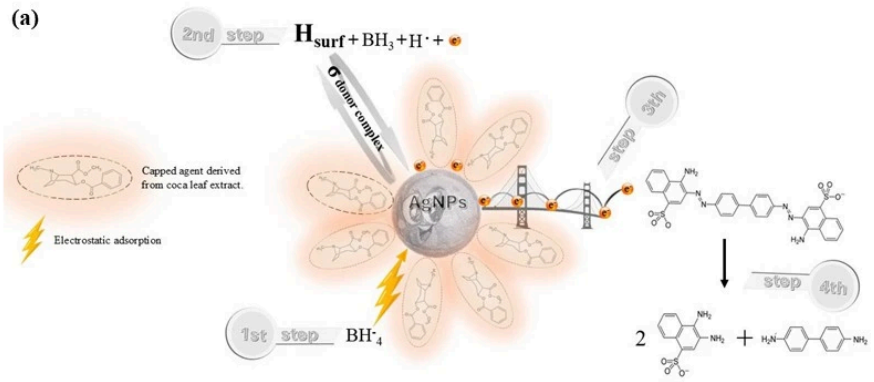


Figure 7. *Cont.*

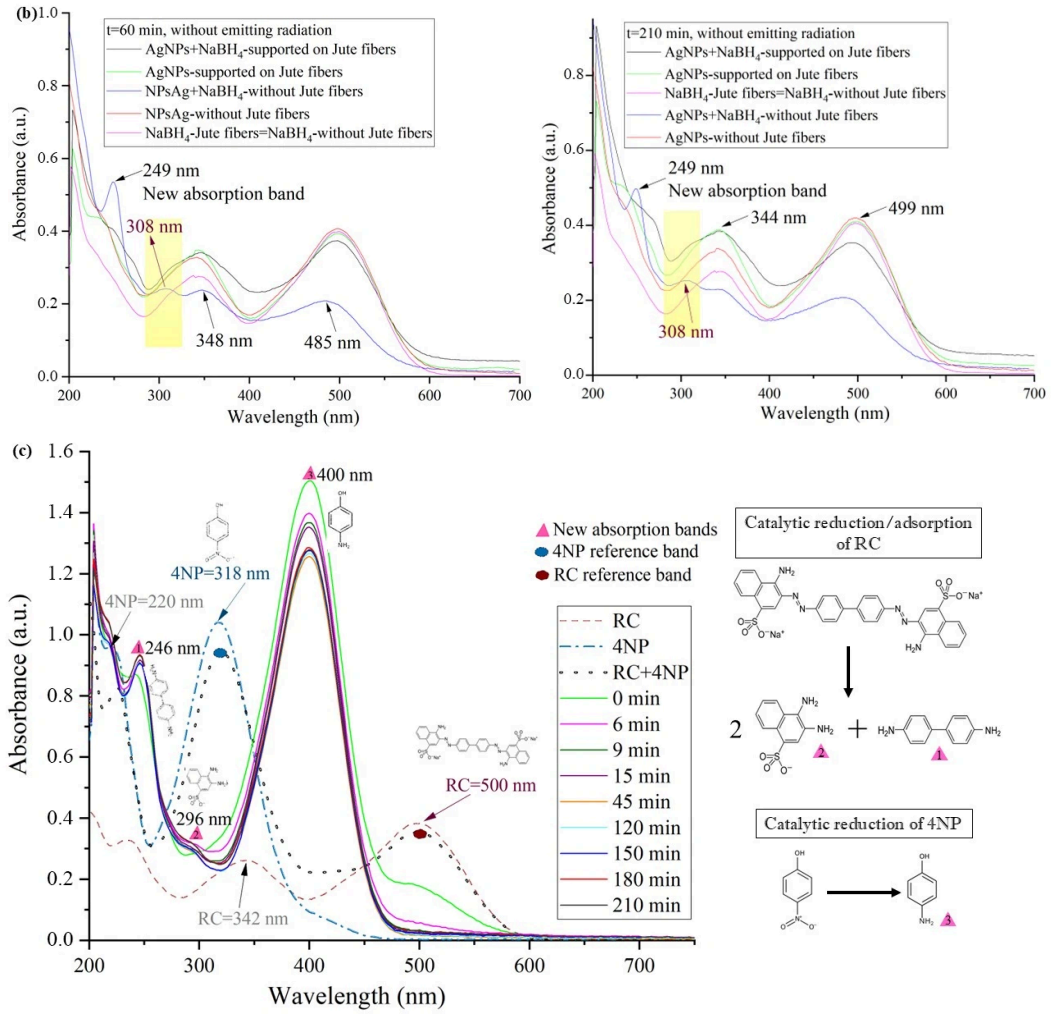


Figure 7. (**a**) Proposed mechanism for the degradation of CR dye and (**b**) removal/degradation kinetics of supported and unsupported systems in Jute fiber and (**c**) removal of multicomponent CR and 4NP pollutants with AgNPs+$NaBH_4$-Jute fiber.

3.4.2. Incorporation of the Ag-NPs into Jute Fibers

The literature reports that nanoparticles can function more efficiently when supported on a biopolymeric matrix [74]. Among other advantages, the matrix may control its growth through its surface accessibility [75]. Confirmation that the nanoparticles had been incorporated into the jute fibers was obtained by analyzing the SEM micrographs taken of the fiber alone and of the fiber with the Ag-NPs attached (Figure 8a–f). The fibers were characterized by a fairly smooth surface, with few cavities or pores (Figure 8a,b), and the chemical elements associated with lignocellulosic materials: C and O; the others correspond to impurities in the material. In contrast, this became rougher due to the deposition of nanoparticles (Figure 8d), which were evenly distributed across the entire surface (Figure 8f). Their concentration did not exceed 1% (Figure 8e); however, for the intended application, these obtained concentrations were tested without pushing the system to achieve higher deposition levels.

Figure 7b shows the behavior of the systems at 60 min. When the nanoparticles are supported on jute fibers (AgNPs+$NaBH_4$-Jute fibers), low intensity peaks at 249 and 380 nm are observed. However, they are more intense in the system without matrix support (AgNPs+$NaBH_4$-without Jute fibers). These peaks are associated with the fragmentation of the CR molecules, as previously mentioned. This means that in AgNPs+$NaBH_4$-Jute fibers, the predominant process is the adsorption of the dye onto the matrix. This process

became more efficient, likely due to the greater availability of adsorption sites on the CR. Additionally, the silver nanoparticles serve as a limited platform for electron transfer; instead, they provide active adsorption sites, similar to those of Jute fibers. Perhaps the nanoparticles coordinated to functional groups on the jute (-OH, -COOH, etc.) and became clogged, thereby reducing electron transfer from BH_4^- to the Ag-NPs and from the Ag-NPs to the CR dye molecules. Reduction experiments using only borohydride, both with and without the fibers, showed no change in the decrease in absorbance at the characteristic CR peaks, indicating that the support does not influence this process. When the nanoparticles are supported without the addition of the reducing agent (AgNPs-Jute fibers), this is still more favorable for the removal of the dye than the unsupported nanoparticles system, only in their colloidal form in solution (AgNPs-without Jute fibers), confirming that new interactions and synergistic effects are generated with the fiber, which lowers the levels of dye in solution.

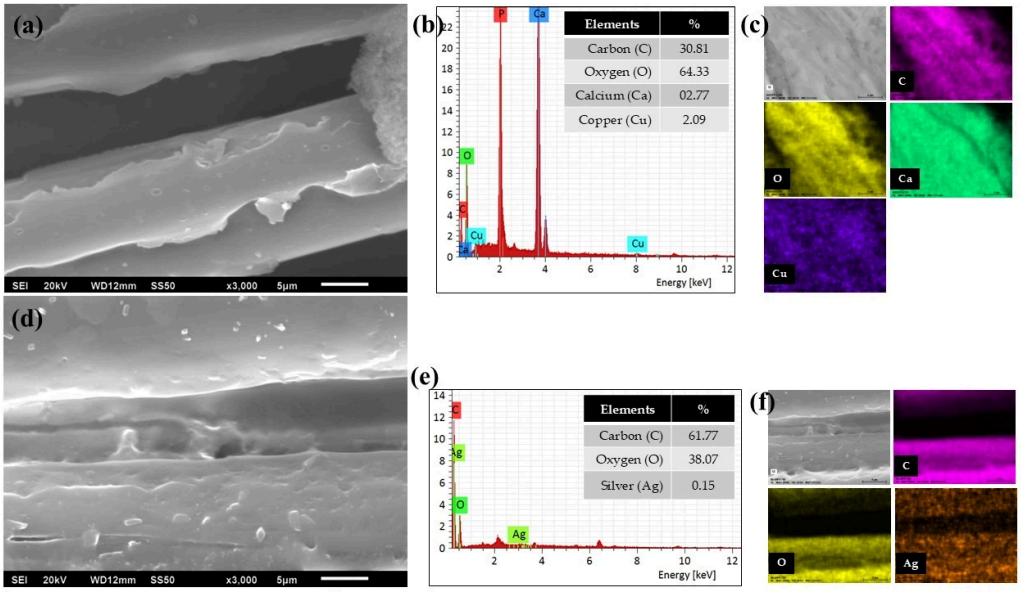


Figure 8. Sem micrographs (**a**,**d**), EDS analysis (**b**,**e**) and Chemical maps (**c**,**f**) of Jute fibers and AgNP–Jute fibers, respectively.

3.4.3. Congo Red/4-Nitrophenol Multicomponent System Degradation Using AgNPs-Jute Fibers

The study of multicomponent systems is a critical issue in this type of research, as real wastewater contains multiple contaminants simultaneously. The presence of multiple species can lead to competition for active sites and alter the efficiency of adsorption or degradation. These studies allow for the evaluation of the material's selectivity and actual performance under conditions closer to real-world environmental applications. Furthermore, they help identify synergistic or antagonistic effects between pollutants. As a result, they provide a more realistic perspective for the design of water treatment technologies [76].

Figure 7c shows the results of experiments on the effect of the presence of another contaminant in the solution. The wavelengths for the absorption peaks of CR and 4NP dissolved in water are clearly defined. But when both components are dissolved in the same volume of water, the evolution of the experiment can only be followed after the addition of $NaBH_4$, as observed at wavelengths of 318 and 500 nm.

After 6 min of contact between the multicomponent solution with the reducing agent and the AgNPs+$NaBH_4$-Jute fiber, three new bands appear (1, 2, and 3), indicating that the catalytic reaction occurs rapidly. The highest intensity is observed for the absorption band

at 400 nm (3). According to García-Romero et al. [55], it is associated with the deprotonation of 4NP and passes to the intermediate 4-nitrophenolate ($4NP^-$) due to the highly basic pH.

The other two new bands (246 and 296 nm) have relatively low intensities, consistent with the explanation above regarding the efficiency of catalytic reduction of the CR when the nanoparticles are supported on the matrix. Even in this context, dye adsorption is usually favored over catalysis. However, the amount of $NaBH_4$ used in the experiment was evidently greater than that required to achieve the catalytic reduction of only one contaminant. This must be the main reason for the more pronounced presence of the adsorption bands of the molecules produced by the fragmentation of the CR (1 and 2), compared with when only the CR was present in solution (Figure 7b). That is, when the nanoparticles are supported on the Jute fiber, the catalytic reduction of the dye no longer predominates; it is still removed by adsorption, even when another contaminant is present in the dye's environment; dye removal remains the primary factor. Therefore, by immobilizing the colloidal nanoparticles in the biopolymeric matrix, they become more efficient at removing both contaminants through multiple simultaneous mechanisms.

3.4.4. Antimicrobial Testing of Ag-NPs

Although pulsed-laser irradiation produced more uniform, near-spherical particles, the antimicrobial response did not systematically improve compared with the non-irradiated colloids. Initial soft-agar overlay tests against *E. coli* indicated that pulsed-laser irradiation did not enhance antibacterial activity and, under comparable conditions, tended to reduce it. In these preliminary assays, the non-irradiated AgNPs produced larger halo inhibition diameters (44.9, 49.81, and 43.94 mm) than the corresponding irradiated systems (37.39 and 43.22 mm). This behavior is consistent with plant-mediated systems, where extract-derived metabolites act as both reducing and stabilizing agents and form an organic capping layer that can modulate nanoparticle–bacteria interactions. In some cases, this capping contributes positively (e.g., improved colloidal stability and synergistic surface chemistry), while in others it can reduce effective surface accessibility and attenuate the delivery of silver at the interface [77,78].

After irradiation, changes in surface chemistry and charge/charge and in the extract-derived capping layer may occur, thereby modifying nanoparticle–cell interactions and the effective availability of silver species. In green Ag-NPs, this biomolecule-derived capping is a key determinant of antibacterial (and often antibiofilm) behavior, so post-treatments that alter surface functionality can shift activity even when morphology changes are moderate. Therefore, the antimicrobial response is not expected to depend solely on morphology, but on the balance among capping, colloidal stability, and surface accessibility [79,80].

Although Carpio et al., [49] demonstrated that laser irradiation can reduce the size and homogenize the spherical morphology of silver nanoparticles, thereby inducing various processes (as mentioned above), the study did not address the biological implications of these modifications. In the research we present, although a smaller reduction in particle size was observed, it was insufficient to confer high antimicrobial activity, indicating that other factors play an equally important role in this application.

Studies reported by Kabeya et al. [81] state that the presence of metabolites in nanoparticles synthesized using the green method not only acts as reducing and stabilizing agents but also as modulators of biological activity, which may have occurred in the present study when the extract derived from *Erythroxylum coca* was used. Similarly, Ferreira et al. [82] reported that coating agents can alter colloidal stability, the release of silver ions, and the interactions that may occur between the nanoparticles and bacteria, directly affecting the antimicrobial response. On the other hand, recent studies indicate that the antibacterial activity of AgNPs synthesized by green methods depends on a combination of size, surface

chemistry, oxidation state, and bioavailability of silver species, even more so than on their isolated morphology [67].

It can therefore be concluded that the active agents present in the extracts of *Erythroxylum coca* tea residues may form an active organic layer on the surface of the silver nanoparticles. This layer may have been altered during irradiation, thereby reducing the synergistic effects responsible for bacterial inhibition [81,82]. Thus, although irradiation has been shown to promote a more homogeneous size distribution, it could also modify surface accessibility or the release of active silver species, offsetting the benefits of size reduction.

Given the colloidal nature of the samples, antimicrobial activity was evaluated using the soft-agar overlay format, and inhibition halos were quantified as area (mm^2) due to the frequent occurrence of irregular inhibition shapes, as reported previously for similar assays [83,84]. As shown in Figure 9, Ag-NPs produced using diluted extracts (1:10 and 1:20) yielded significantly larger inhibition areas ($p < 0.005$), typically in the ~60–120 mm^2 range, compared with Ag-NPs prepared with the undiluted extract and the $AgNO_3$ control, which mostly ranged between ~45–80 mm^2. The inhibition response was strain-dependent; notably, for HHM 25 and *E. coli* ATCC 25922, Ag-NPs biosynthesized with undiluted extract were not significantly different from $AgNO_3$, whereas both diluted-extract systems showed significant differences versus the control. Overall, these results indicate that antimicrobial performance was favored when Ag-NPs were produced using diluted extracts, consistent with a less-passivating capping layer enabling improved nanoparticle–bacteria contact and effective silver delivery; notably, *Erythroxylum* extracts have been reported to be rich in phenolics/flavonoids that can act as reducing/capping agents [85], and related plant-mediated systems show that extract composition can tune Ag-NPs surface chemistry/colloidal properties and translate into measurable differences in antibacterial performance [86].

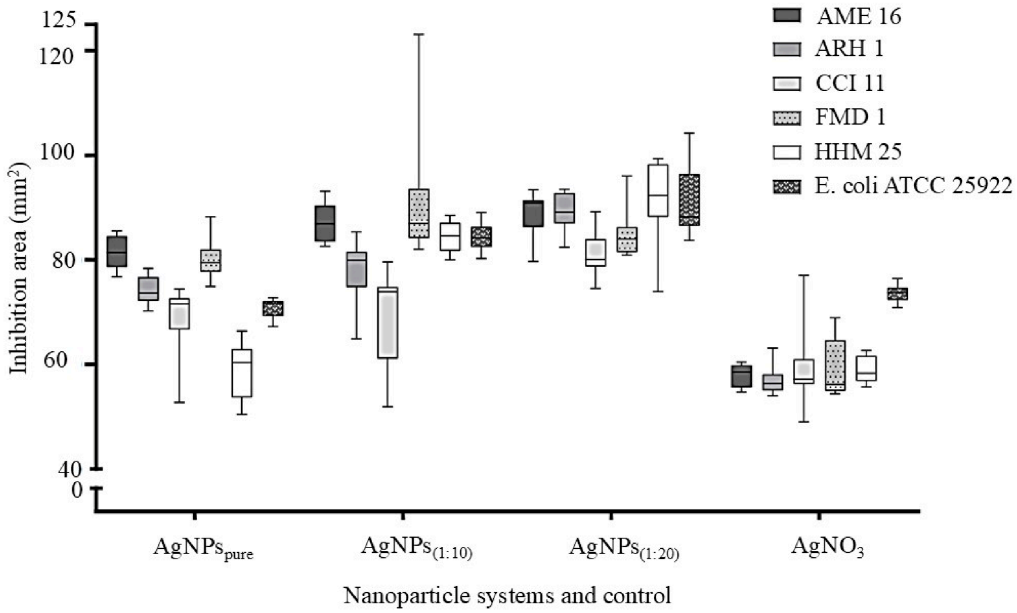


Figure 9. Box plot of the inhibition zone under three types of colloidal Ag-NPs and the silver nitrate control in six bacterial strains.

3.4.5. Inhibition of Biofilm Formation

Biofilm inhibition was quantified by the crystal-violet microtiter assay after 24 h exposure to three Ag-NPs formulations (pure extract, 1:10, 1:20) and an $AgNO_3$ control at MIC-normalized doses [50,51]. Overall, all silver treatments reduced crystal-violet

biomass relative to the growth control, and inhibition increased from 0.5 × MIC to 1 × MIC (Figure 10a).

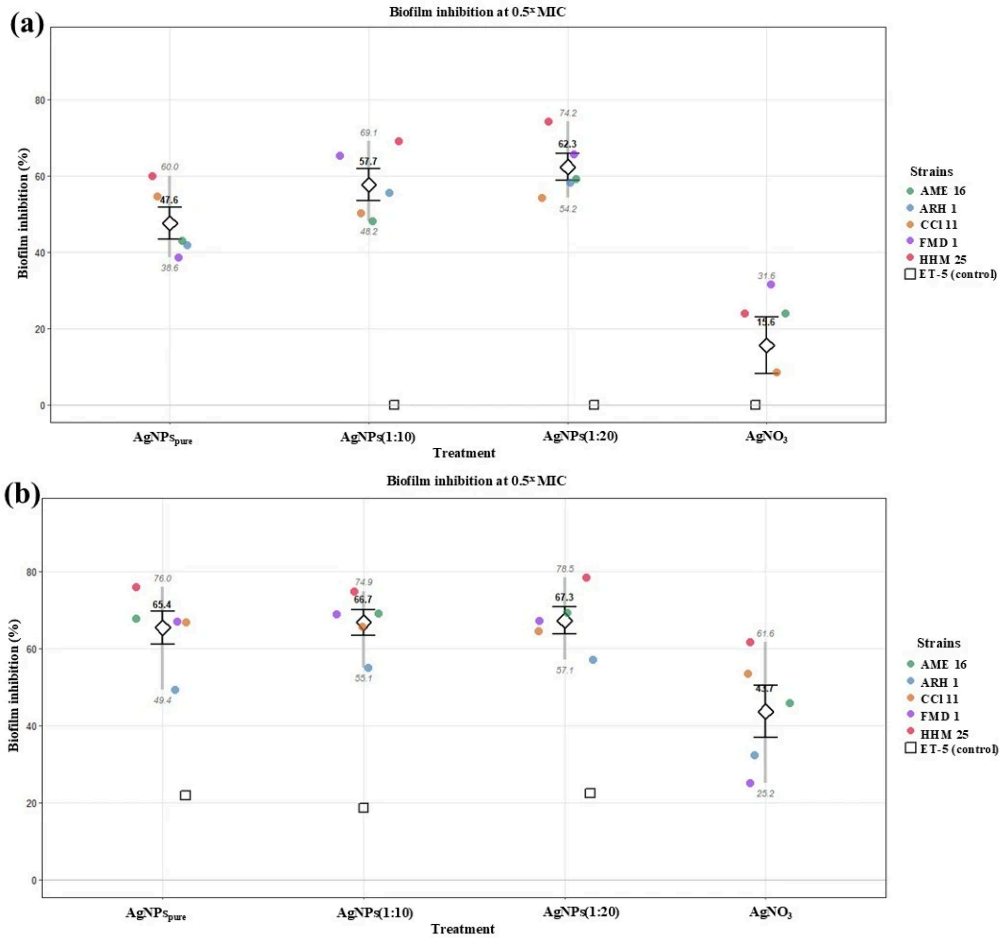


Figure 10. Biofilm inhibition at 0.5 × MIC and 1 × MIC. Biofilm biomass inhibition (%) was quantified by the crystal violet microtiter assay after 24 h and expressed as the percent reduction in OD_{570} relative to the growth control. Panels show inhibition at (**a**) 0.5 × MIC and (**b**) 1 × MIC for $AgNPs_{pure}$, Ag-NPs (1:10), AgNPs (1:20), and $AgNO_3$. Points represent individual strains (AME 16, ARH 1, CCI 11, FMD 1, and HHM 25), with *E. coli* ATCC 25922 included as a biofilm-forming control and ET5 as a non-biofilm control; diamonds indicate the mean across biofilm-forming strains.

At 0.5 × MIC, all Ag-NP formulations showed substantially higher inhibition than $AgNO_3$ (mean inhibition ~47.6–62.3% for AgNPs vs. ~15.6% for $AgNO_3$), with the diluted systems (1:10 and 1:20) trending higher than the pure-extract Ag-NPs. At 1 × MIC (Figure 10b), inhibition increased, and the three Ag-NP systems converged (~65.4–67.3%), while $AgNO_3$ also increased (~43.7%), comparing nanoparticulate and ionic silver. The biofilm-forming control (*E. coli* ATCC 25922) responded within the range of the biofilm-forming strain panel, whereas the non-biofilm control (ET5) remained low across treatments, consistent with its phenotype and supporting that the assay primarily captures biofilm biomass modulation rather than only planktonic growth effects.

This dose-dependent trend, in which treatment differences are more pronounced below MIC and diminish near MIC, is consistent with reports that Ag-NP antibiofilm performance depends strongly on surface chemistry and colloidal presentation during early biofilm development, when nanoparticles can interfere with initial adhesion and EPS (extracellular polymeric substance) assembly, while higher silver exposures suppress biomass regardless of presentation [39–41]. Proposed Ag-NP–biofilm interactions include electrostatic/hydrophobic contacts and disruption of EPS components (polysaccharides,

proteins, and nucleic acids), which can yield strain-dependent responses [87,88]. Given the relevance of biofilms to persistence and recurrence in uropathogenic/ExPEC infections [38,39,89], the measurable inhibition observed at sub-MIC/MIC-equivalent exposure supports the microbiological relevance of the Ag-NPs formulations in addition to their planktonic antibacterial readout.

4. Conclusions

Our findings demonstrate that *Erythroxylum coca* leaf extract effectively serves as a dual-role reducing and stabilizing agent, facilitating a fully biogenic, room-temperature synthesis of silver nanoparticles without external chemical additives. The resulting nanoparticles displayed a broad surface plasmon resonance band, indicative of significant size and morphological heterogeneity within the colloidal population, thereby providing a suitable starting point for subsequent laser-assisted refinement. Laser-assisted processing promoted morphological and size homogenization, resulting in a predominantly spherical nanoparticle population with a narrower size distribution, as evidenced by the SPR band, which was between 404 and 410 nm. Moreover, irradiation appeared to increase the nanoparticle concentration while preserving size stability, highlighting its effectiveness as a reagent-free post-synthetic refinement strategy. Despite their different formation mechanisms, the biogenically synthesized and laser-refined Ag-NPs exhibited similar catalytic efficiencies, underscoring the robustness of their catalytic functionality. The high catalytic efficiency of the green-synthesized Ag-NPs can be attributed to residual bioactive constituents from the *Erythroxylum coca* extract, which function as natural stabilizing and surface-modifying agents, thereby increasing the availability of catalytically active sites. By contrast, the laser-irradiated Ag-NPs derived their catalytic effectiveness from enhanced structural uniformity and colloidal stability. These distinct yet complementary characteristics resulted in comparable dye-degradation performance. In antimicrobial applications, however, the narrower size distribution and greater morphological homogeneity of the irradiated nanoparticles are expected to favor stronger and more reproducible interactions with bacterial membranes, potentially leading to improved antimicrobial activity. Nevertheless, the superior antimicrobial and antibiofilm performance of the green-synthesized Ag-NPs can be attributed to the presence of phytochemicals derived from the *Erythroxylum coca* extract that are retained on the nanoparticle surface. These bioactive molecules likely act synergistically with the Ag-NPs, enhancing nanoparticle–bacteria interactions, promoting membrane destabilization, and facilitating antimicrobial action. Finally, the Ag/jute nanocomposites demonstrated outstanding catalytic performance, efficiently degrading Congo red dye and facilitating concurrent degradation/reduction pathways in multicomponent systems containing Congo red and 4-nitrophenol. These results highlight their ability to address the complexity of real wastewater streams, where multiple contaminants often coexist and interact. Furthermore, the synthesized Ag-NPs exhibited pronounced antimicrobial activity against *Escherichia coli*, revealing their potential to simultaneously mitigate chemical and biological pollutants. Collectively, these findings establish the Ag/jute nanocomposite platform as a multifunctional and sustainable material for environmental remediation. More broadly, this work demonstrates how integrating agricultural waste valorization, green nanotechnology, and laser-assisted nanoparticle engineering can produce high-value materials with enhanced functionality and reusability, offering a promising pathway toward next-generation technologies for water purification, wastewater treatment, and antimicrobial control.

Author Contributions: Conceptualization A.B.F. and D.R.C., Investigation Y.D.Z., M.B.I., D.M.Á.M. and A.R.V.N.; validation M.A.C.L., C.C.T. and D.M.Á.M.; methodology C.C.T. and D.M.Á.M.; formal analysis D.R.C. and H.P.T.J.; data curation H.P.T.J. and S.G.C.; writing—original draft preparation A.B.F. and D.R.C.; writing—review and editing H.P.T.J., S.G.C. and D.R.C.; visualization C.C.T. and

S.G.C.; supervision C.C.T. and A.B.F.; project administration A.B.F.; funding acquisition A.B.F. All authors have read and agreed to the published version of the manuscript.

Funding: This research was supported by the Consejo Mexiquense de Ciencia y Tecnología (COMECYT) through financing granted to the FICDTEM-2023-142, also by Tecnológico de Estudios Superiores de Tianguistenco (TEST) through financing granted to the DIDT/CI2025/18 project. And for the scholarship awarded within the framework of the "COMECYT Researchers Program" project with reference number CAT2025-0021.

Data Availability Statement: Data will be made available on request.

Acknowledgments: The authors also thank the TEST, IBMB, for the lab facilities to carry out the experiments. We would like to express our gratitude to SEHCITI for the scholarship awarded to Yeshua Díaz Zamora for the development of his master's degree. During the preparation of this manuscript/study, the authors used OpenAI ChatGPT (Modelo GPT-5 con DALL·E) for the purposes of Figure 4 and Graphical Abstract. The authors have reviewed and edited the output and take full responsibility for the content of this publication.

Conflicts of Interest: The authors declare no conflicts of interest.

References

1. Turkevich, J.; Cooper Stevenson, P.; Hillier, J. A study of the nucleation and growth processes in the synthesis of colloidal gold. *Discuss. Faraday Soc.* **1951**, *11*, 55–75. [CrossRef]
2. Abbas, R.; Luo, J.; Qi, X.; Naz, A.; Khan, I.A.; Liu, H.; Yu, S.; Wei, J. Silver nanoparticles: Synthesis, structure, properties and applications. *Nanomaterials* **2024**, *14*, 1425. [CrossRef] [PubMed]
3. Kim, S.M.; Choi, H.J.; Lim, J.A.; Woo, M.A.; Chang, H.J.; Lee, N.; Lim, M.C. Biosynthesis of silver nanoparticles from Duchesnea indica extracts using different solvents and their antibacterial activity. *Microorganisms* **2023**, *11*, 1539. [CrossRef] [PubMed]
4. Sati, A.; Ranade, T.N.; Mali, S.N.; Ahmad Yasin, H.K.; Pratap, A. Silver nanoparticles (AgNPs): Comprehensive insights into bio/synthesis, key influencing factors, multifaceted applications, and toxicity—A 2024 update. *ACS Omega* **2025**, *10*, 7549−7582. [CrossRef]
5. Akdasçi, E.; Eker, F.; Duman, H.; Bechelany, M.; Karav, S. Microbial-based green synthesis of silver nanoparticles: A comparative review of bacteria- and fungi-mediated approaches. *Int. J. Mol. Sci.* **2025**, *26*, 10163. [PubMed]
6. Dheyab, M.A.; Aziz, A.A.; Nowfal, S.H.; Braim, F.S.; Abdullah, W.; Kasasbeh, W.H.; Mahmood, S.J.; Alanezi, S.T.; Alrosan, M.; Oladzadabbasabadi, N. Sustainable green synthesis of silver nanoparticles for safer biomedical application. *J. Environ. Chem. Eng.* **2025**, *13*, 115998. [CrossRef]
7. Bhatu, M.N.; Mavlankar, G.R.; Baviskar, R.; Patil, A.B.; Patil, S.P. Ag-based bimetallic nanoparticles for the catalytic reduction of nitrophenol and organic dyes: An overview. *ChemistrySelect* **2024**, *9*, e202304200. [CrossRef]
8. Hosny, S.; Gaber, G.A.; Ragab, M.S.; Ragheb, M.A.; Anter, M.; Mohamed, L.Z. A Comprehensive review of silver nanoparticles (AgNPs): Synthesis strategies, toxicity concerns, biomedical applications, AI-driven advancements, challenges, and future perspectives. *Arab. J. Sci. Eng.* **2026**, *51*, 13667–13714. [CrossRef]
9. Dube, E.; Okuthe, G.E. Silver nanoparticle-based antimicrobial coatings: Sustainable strategies for microbial contamination control. *Microbiol. Res.* **2025**, *16*, 110. [CrossRef]
10. Faghani, G.; Azarniya, A. Emerging nanomaterials for novel wound dressings: From metallic nanoparticles and MXene nanosheets to metal-organic frameworks. *Heliyon* **2024**, *10*, e39611. [CrossRef] [PubMed]
11. Chabuk, S.K.; Naji, R.J.; Mohammed, L.H.; Al-fahham, A.A. Updates for silver nanoparticles' applications in medical field: A review article. *Int. J. Med. Sci. Dent. Health* **2025**, *11*, 41–47. [CrossRef]
12. Antiochia, R.; Bollella, P.; Favero, G.; Mazzei, F. Nanotechnology-based surface plasmon resonance affinity biosensors for in vitro diagnostics. *Int. J. Anal. Chem.* **2016**, *2016*, 2981931. [CrossRef] [PubMed]
13. Kumar, A.; Savanur, M.R.S.; Singh, S.K.; Singh, J.; Bhattacharya, S.; Asnani, K.; Kumar, S. Recent advances in silver nanoparticles-catalyzed reactions. *ChemistrySelect* **2025**, *10*, e202403655. [CrossRef]
14. Krishna, S.B.N.; Sheik, A.G.; Pillay, K.; Hamza, M.A.; Elamir, M.Y.M.; Selim, S. Nanotechnology in action: Silver nanoparticles for improved eco-friendly remediation. *PeerJ* **2024**, *12*, e18191. [CrossRef] [PubMed]
15. Fahim, M.; Shahzaib, A.; Nishat, N.; Jahan, A.; Bhat, T.A.; Inam, A. Green synthesis of silver nanoparticles: A comprehensive review of methods, influencing factors, and applications. *JCIS Open* **2024**, *16*, 100125. [CrossRef]
16. Parveen, K.; Banse, V.; Ledwani, L. Green synthesis of nanoparticles: Their advantages and disadvantages. In *AIP Conference Proceedings*; AIP Publishing: Melville, NY, USA, 2016; Volume 1724.

17. Rajeshkumar, S.; Sivapriya, D. Fungus-mediated nanoparticles: Characterization and biomedical advances. In *Nanoparticles in Medicine*; Springer: Singapore, 2020; pp. 185–199.
18. Yadav, A.; Kon, K.; Kratosova, G.; Duran, N.; Ingle, A.P.; Rai, M. Fungi as an efficient mycosystem for the synthesis of metal nanoparticles: Progress and key aspects of research. *Biotechnol. Lett.* **2015**, *37*, 2099–2120. [CrossRef] [PubMed]
19. Shah, M.; Fawcett, D.; Sharma, S.; Tripathy, S.K.; Poinern, G.E.J. Green synthesis of metallic nanoparticles via biological enti-ties. *Materials* **2015**, *8*, 7278–7308. [CrossRef] [PubMed]
20. Pal, G.; Rai, P.; Pandey, A. Green synthesis of nanoparticles: A greener approach for a cleaner future. In *Green Synthesis, Char-Acterization and Applications of Nanoparticles*; Shukla, A.K., Iravani, S., Eds.; Elsevier: Amsterdam, The Netherlands, 2019; pp. 1–26.
21. Ahmed, S.; Ahmad, M.; Swami, B.L.; Ikram, S. Green synthesis of silver nanoparticles using Azadirachta indica aqueous leaf extract. *J. Radiat. Res. Appl. Sci.* **2016**, *9*, 1–7. [CrossRef]
22. Kalimuthu, K.; Babu, R.S.; Venkataraman, D.; Bilal, M.; Gurunathan, S. Biosynthesis of silver nanocrystals by Bacillus licheniformis. *Colloids Surf. B* **2008**, *65*, 150–153. [CrossRef]
23. Liu, D.; Li, C.; Zhou, F.; Zhang, T.; Zhang, H.; Li, X.; Li, Y. Rapid synthesis of monodisperse Au nanospheres through a laser irradiation-induced shape conversion, self-assembly and their electromagnetic coupling SERS enhancement. *Sci. Rep.* **2015**, *5*, 7686. [CrossRef] [PubMed]
24. Tsuji, T.; Kikuchi, M.; Kagawa, T.; Adachi, H.; Tsuji, M. Morphological changes from spherical silver nanoparticles to cubes after laser irradiation in acetone–water solutions via spontaneous atom transportation process. *Colloids Surf. A* **2017**, *529*, 33–37. [CrossRef]
25. Tajdidzadeh, M.; Azmi, B.Z.; Yunus, W.M.M.; Talib, Z.A.; Sadrolhosseini, A.R.; Karimzadeh, K.; Dorraj, M. Synthesis of silver nanoparticles dispersed in various aqueous media using laser ablation. *Sci. World J.* **2014**, *2014*, 324921. [CrossRef]
26. Biondich, A.S.; Joslin, J.D. Coca: The history and medical significance of an ancient andean tradition. *Emerg. Med. Int.* **2016**, *2016*, 4048764. [CrossRef] [PubMed]
27. Wang, Z.; Ahmad, W.; Zhu, A.; Zhao, S.; Ouyang, Q.; Chen, Q. Recent advances review in tea waste: High-value applications, processing technology, and value-added products. *Sci. Total Environ.* **2024**, *946*, 174225. [CrossRef] [PubMed]
28. Çakmak, T.G.; Saricaoglu, B.; Ozkan, G.; Tomas, M.; Capanoglu, E. Valorization of tea waste: Composition, bioactivity, extraction methods, and utilization. *Food Sci. Nutr.* **2024**, *12*, 3112–3124. [CrossRef] [PubMed]
29. Rabbi, M.A.; Rahman, M.M.; Minami, H.; Yamashita, N.; Habib, M.R.; Ahmad, H. Magnetically responsive antibacterial nano-crystalline jute cellulose nanocomposites with moderate catalytic activity. *Carbohydr. Polym.* **2021**, *51*, 117024. [CrossRef]
30. Kumar, P.; Dixit, J.; Singh, A.K.; Rajput, V.D.; Verma, P.; Tiwari, K.N.; Mishra, S.K.; Minkina, T.; Mandzhieva, S. Efficient catalytic degradation of selected toxic dyes by green biosynthesized silver nanoparticles using aqueous leaf extract of *Cestrum nocturnum* L. *Nanomaterials* **2022**, *12*, 3851. [CrossRef] [PubMed]
31. Ivanovska, A.; Branković, I.; Lađarević, J.; Pavun, L.; Kostic, M. Oxidized jute as a valuable adsorbent for Congo Red from an aqueous solution. *J. Eng. Fibers Fabr.* **2022**, *17*, 15589250221101380. [CrossRef]
32. Altakroury, A.R.; Gatsa, O.; Riahi, F.; Fu, Z.; Flimelová, M.; Samokhvalov, A.; Barcikowski, S.; Doñate-Buendía, C.; Bulgakov, A.V.; Gökce, B. Size control of nanoparticles synthesized by pulsed laser ablation in liquids using donut-shaped beams. *Beilstein J. Nanotechnol.* **2025**, *16*, 407–417. [CrossRef] [PubMed]
33. Qazi, U.Y.; Shervani, Z.; Javaid, R. Green synthesis of silver nanoparticles by pulsed laser irradiation: Effect of hydrophilicity of dispersing agents on size of particles. *Front. Nanosci. Nanotechnol.* **2018**, *4*, 61–69. [CrossRef]
34. Elia, B.C.; Morales, M.A.; Franco, V.G.; García, J.A.F.; Goya, G.F. Magnetically enhanced Fenton-like processes by nanofibers: Real-time observation of tetracycline degradation in pig manure wastewater. *arXiv* **2025**, arXiv:2504.20087.
35. Khalil, A.M.; Kamel, S.; Mohy-Eldin, M.S. Photocatalytic degradation of Congo red dye using innovative cerium titanate nanorods embedded in a cellulose-based hydrogel. *Sci. Rep.* **2026**, *16*, 12476. [CrossRef] [PubMed]
36. Dhila, H.; Bhapkar, A.; Bhame, S. Metal oxide/biochar hybrid nanocomposites for adsorption and photocatalytic degradation of textile dye effluents: A review. *Desalin. Water Treat.* **2025**, *321*, 101004. [CrossRef]
37. Sarowska, J.; Futoma-Koloch, B.; Jama-Kmiecik, A.; Frej-Madrzak, M.; Ksiazczyk, M.; Bugla-Ploskonska, G.; Choroszy-Krol, I. Virulence factors, prevalence and potential transmission of extraintestinal pathogenic Escherichia coli isolated from different sources: Recent reports. *Gut Pathog.* **2019**, *11*, 10. [CrossRef] [PubMed]
38. Baldiris-Avila, R.; Montes-Robledo, A.; Buelvas-Montes, Y. Phylogenetic classification, biofilm-forming capacity, virulence factors, and antimicrobial resistance in uropathogenic Escherichia coli (UPEC). *Curr. Microbiol.* **2020**, *77*, 3361–3370. [CrossRef] [PubMed]
39. Hall-Stoodley, L.; Costerton, J.W.; Stoodley, P. Bacterial biofilms: From the natural environment to infectious diseases. *Nat. Rev. Microbiol.* **2004**, *2*, 95–108. [CrossRef] [PubMed]
40. Dizaj, S.M.; Lotfipour, F.; Barzegar-Jalali, M.; Zarrintan, M.H.; Adibkia, K. Antimicrobial activity of the metals and metal oxide nanoparticles. *Mater. Sci. Eng. C* **2014**, *44*, 278–284. [CrossRef]

41. Rai, M.; Yadav, A.; Gade, A. Silver nanoparticles as a new generation of antimicrobials. *Biotechnol. Adv.* **2009**, *27*, 76–83. [CrossRef] [PubMed]
42. Kalishwaralal, K.; BarathManiKanth, S.; Pandian, S.R.K.; Deepak, V.; Gurunathan, S. Silver nanoparticles impede the biofilm formation by Pseudomonas aeruginosa and Staphylococcus epidermidis. *Colloids Surf. B* **2010**, *79*, 340–344. [CrossRef]
43. Joshi, A.S.; Singh, P.; Mijakovic, I. Interactions of gold and silver nanoparticles with bacterial biofilms: Molecular interactions behind inhibition and resistance. *Int. J. Mol. Sci.* **2020**, *21*, 7658. [CrossRef] [PubMed]
44. Li, H.; Yang, Z.; Khan, S.A.; Walsh, J.L.; Seneviratne, C.J.; Ziora, Z.M. Characteristics of metallic nanoparticles (Especially silver nanoparticles) as anti-biofilm agents. *Antibiotics* **2024**, *13*, 819. [CrossRef] [PubMed]
45. Durán, N.; Marcato, P.D.; Alves, O.L.; De Souza, G.I.; Esposito, E. Mechanistic aspects of biosynthesis of silver nanoparticles by several Fusarium oxysporum strains. *J. Nanobiotechnol.* **2005**, *3*, 8. [CrossRef]
46. Nikolov, A.S.; Stankova, N.E.; Karashanova, D.B.; Nedyalkov, N.N.; Pavlov, E.L.; Koev, K.T.; Najdenskid, H.R.; Kussovskid, V.; Avramova, L.A.; Ristoscue, C.; et al. Synergistic effect in a two-phase laser procedure for production of silver nanoparticles colloids applicable in ophthalmology. *Opt. Laser Technol.* **2021**, *38*, 106850.
47. Jain, R.; Vidhani, B.; Tyagi, S.; Jain, R. Silver nanoparticles for antibacterial applications: Current insights and emerging trends. *AIP Adv.* **2026**, *16*, 030702–1–030702–13. [CrossRef]
48. Morales-Luckie, R.A.; Palacios-Lozano, S.L.; Sánchez-Mendieta, V.; Olea-Mejia, O.F.; González-Pedroza, M.G. Bionanoomposite of Ag Nanoparticles/Jute Fibers as an Efficient Fungi-Free Material for the Automobile Industry. In *Vegetable Fiber Composites and Their Technological Applications*; Springer: Singapore, 2021; pp. 327–338.
49. Carpio-Martínez, P.; Ruiz, V.F.; Camacho-López, M.A.; Sánchez-Mendieta, V.; Vilchis-Nestor, A.R. Morphological and size tuning of biogenic Ag and Au nanoparticles induced by laser irradiation. *Phys. Scr.* **2024**, *99*, 055940. [CrossRef]
50. EUCAST. *Breakpoint Tables for Interpretation of MICs and Zone Diameters*, Version 12.0; EUCAST: Växjö, Sweden, 2022.
51. Hockett, K.L.; Baltrus, D.A. Use of the soft-agar overlay technique to screen for bacterially produced inhibitory compounds. *JoVE J. Vis. Exp.* **2017**, *119*, e55064. [CrossRef]
52. Schneider, C.A.; Rasband, W.S.; Eliceiri, K.W. NIH Image to ImageJ: 25 years of image analysis. *Nat. Methods* **2012**, *9*, 671–675. [CrossRef] [PubMed]
53. Barabadi, H.; Mojab, F.; Vahidi, H.; Marashi, B.; Talank, N.; Hosseini, O.; Saravanan, M. Green synthesis, characterization, anti-bacterial and biofilm inhibitory activity of silver nanoparticles compared to commercial silver nanoparticles. *Inorg. Chem. Commun.* **2021**, *129*, 108647. [CrossRef]
54. Wiegand, I.; Hilpert, K.; Hancock, R.E. Agar and broth dilution methods to determine the minimal inhibitory concentration (MIC) of antimicrobial substances. *Nat. Protoc.* **2008**, *3*, 163–175. [CrossRef] [PubMed]
55. Romero, G.G.; Ruíz, V.F.R.; Flores, A.B.; Jaldin, H.P.T.; Vilchis-Nestor, A.R.; Ávila-Márquez, D.M.; Contreras, D.R. Light-driven synthesis of silver nanoparticles using Erythroxylum coca extract for catalytic reduction of 4-nitrophenol. *Biocatal. Agric. Biotechnol.* **2025**, *64*, 103492. [CrossRef]
56. Vidal Gamarra, O.; Fuertes, R.C.; Chávez, S.N.; Contreras, D.C.; Goya, E.S.; Huamantumba, B.K.; Retuerto, P.F.; Ruiz, G.P. Metabolitos detectados en las hojas de Erythroxylum coca Lam. y Erythroxylum novogranatense (Morris) Hieron. y evaluación de sus propiedades biológicas mediante bioensayos. *Rev. Peru. Med. Integr.* **2017**, *2*, 828–834.
57. Ahmad, N.; Sharma, S.; Alam, M.K.; Singh, V.N.; Shamsi, S.F.; Mehta, B.R.; Fatma, A. Rapid synthesis of silver nanoparticles using dried medicinal plant of basil. *Colloids Surf. B* **2010**, *81*, 81–86. [CrossRef]
58. Mude, N.; Ingle, A.; Gade, A.; Rai, M. Synthesis of silver nanoparticles using callus extract of Carica papaya—A first report. *J. Plant Biochem. Biotechnol.* **2009**, *18*, 83–86.
59. Punjabi, K.; Choudhary, P.; Samant, L.; Mukherjee, S.; Vaidya, S.; Chowdhary, A. Biosynthesis of nanoparticles: A review. *Int. J. Pharm. Sci. Rev. Res.* **2015**, *30*, 219–226.
60. Iravani, S. Green synthesis of metal nanoparticles using plants. *Green Chem.* **2011**, *13*, 2638–2650. [CrossRef]
61. Kumar, I.; Gangwar, C.; Yaseen, B.; Pandey, P.K.; Mishra, S.K.; Naik, R.M. Kinetic and mechanistic studies of the formation of silver nanoparticles by nicotinamide as a reducing agent. *ACS Omega* **2022**, *7*, 13778–13788. [CrossRef] [PubMed]
62. Baker, T.A.; Monti, O.L.; Nesbitt, D.J. Kinetic studies of the photogeneration of silver nanoparticles. *J. Phys. Chem. C* **2011**, *115*, 9861–9870. [CrossRef]
63. Fujitsuka, M.; Majima, T. Reaction dynamics of excited radical ions revealed by femtosecond laser flash photolysis. *J. Photochem. Photobiol. C* **2018**, *35*, 25–37. [CrossRef]
64. Wu, C.; Zhou, X.; Wei, J. Localized surface plasmon resonance of silver nanotriangles synthesized by a versatile solution reac-tion. *Nanoscale Res. Lett.* **2015**, *10*, 354. [CrossRef] [PubMed]
65. Alsulami, M.N.; El-Wakil, E.S. Green synthesis of chitosan/silver nanoparticles using Citrus paradisi extract and its potential anti-cryptosporidiosis effect. *Pharmaceutics* **2024**, *16*, 968. [CrossRef] [PubMed]

66. Becerril, D.; Noguez, C. Adsorption of a methylthio radical on silver nanoparticles: Size dependence. *J. Phys. Chem. C* **2015**, *119*, 10824–10835.
67. Eker, F.; Akdasçi, E.; Duman, H.; Bechelany, M.; Karav, S. Green synthesis of silver nanoparticles using plant extracts: A comprehensive review of physicochemical properties and multifunctional applications. *Int. J. Mol. Sci.* **2025**, *26*, 6222. [CrossRef] [PubMed]
68. Syed, S.M.; Kulkarni, S.; Patil, M.; Satpute, K. A comprehensive review of green synthesis methods and applications of nanoparticles derived from plant extracts and microorganisms. *Discov. Green Chem.* **2026**, *1*, 6. [CrossRef]
69. Miyanda, P.; Parveen, Z. Role of plant phytochemicals in reduction, nucleation and stabilization of metallic nanoparticles in green synthesis. *Int. J. Pharm. Sci.* **2026**, *4*, 2057–2085.
70. OpenAI. ChatGPT (Modelo GPT-5 con DALL·E) [Modelo de Lenguaje e Inteligencia Artificial]. 2026. Available online: https://chat.openai.com/ (accessed on 15 May 2026).
71. Liu, Y.; Zhang, X. Degradation of Congo Red dye with a novel silver nanoparticle-catalyzed reduction process. *J. Environ. Sci.* **2010**, *22*, 738–743.
72. Sachdeva, B.; Aggarwal, K.; Singh, A.; Kumari, K.; Chandra, R.; Singh, S. Advancements in silver-based nanocatalysts for organic transformations and other applications: A comprehensive review (2019–2024). *RSC Adv.* **2025**, *15*, 17591–17634. [CrossRef] [PubMed]
73. Shahzadi, S.; Fatima, S.; Shafiq, Z.; Janjua, M.R.S.A. A review on green synthesis of silver nanoparticles (SNPs) using plant extracts: A multifaceted approach in photocatalysis, environmental remediation, and biomedicine. *RSC Adv.* **2025**, *15*, 3858. [CrossRef] [PubMed]
74. Krishnan, A.; Kanniyappan, P.; Vaithilingam, S.; Govindraj, L.; Muthukaruppan, A. Bio-polymer based thermally stable composites as catalytic support materials for energy harvesting process. *Int. J. Hydrogen Energy* **2024**, *50*, 1484–1495. [CrossRef]
75. Nasrollahzadeh, M.; Bidgoli, N.S.S.; Nezafat, Z.; Shafiei, N. Catalytic applications of biopolymer-based metal nanoparticles. In *Biopolymer-Based Metal Nanoparticle Chemistry for Sustainable Applications*; Elsevier: Amsterdam, The Netherlands, 2021; pp. 423–516.
76. Parniske, J.; Andreas, F.; Morck, T. Modelling competitive adsorption of organic micropollutants onto granular activated carbon in fixed-bed adsorbers for advanced wastewater treatment. *Water Res.* **2025**, *288*, 124631. [CrossRef] [PubMed]
77. Perni, S.; Hakala, V.; Prokopovich, P. Biogenic synthesis of antimicrobial silver nanoparticles capped with l-cysteine. *Colloids Surf. A* **2014**, *460*, 219–224. [CrossRef]
78. Burkowska-But, A.; Sionkowski, G.; Walczak, M. Influence of stabilizers on the antimicrobial properties of silver nanoparticles introduced into natural water. *J. Environ. Sci.* **2014**, *26*, 542–549. [CrossRef]
79. Gorohovs, M.; Dekhtyar, Y. Surface Functionalization of Nanoparticles for Enhanced Electrostatic Adsorption of Biomolecules. *Molecules* **2025**, *30*, 3206. [CrossRef] [PubMed]
80. Mikhailova, E.O. Green silver nanoparticles: An antibacterial mechanism. *Antibiotics* **2025**, *14*, 1092. [CrossRef]
81. Kabeya, J.K.; Ngombe, N.K.; Mutwale, P.K.; Safari, J.B.; Matlou, G.G.; Krause, R.W.; Nkanga, C.I. Antimicrobial capping agents on silver nanoparticles made via green method using natural products from banana plant waste. *Artif. Cells Nanomed. Biotechnol.* **2025**, *53*, 29–42. [CrossRef] [PubMed]
82. Ferreira, A.M.; Vikulina, A.; Loughlin, M.; Volodkin, D. How similar is the antibacterial activity of silver nanoparticles coated with different capping agents? *RSC Adv.* **2023**, *13*, 10542–10555. [CrossRef] [PubMed]
83. Mohanaparameswari, S.; Balachandramohan, M.; Sasikumar, P.; Rajeevgandhi, C.; Vimalan, M.; Pugazhendhi, S.; Krishnamurthy, G.; Albukhaty, S.; Salaiman, G.; Abomughaid, M.; et al. Investigation of structural properties and antibacterial activity of AgO nanoparticle extract from Solanum nigrum/Mentha leaf extracts by green synthesis method. *Green Process. Synth.* **2023**, *12*, 20230080. [CrossRef]
84. Hosnedlova, B.; Kabanov, D.; Kepinska, M.; Narayanan, V.H.; Parikesit, A.A.; Fernandez, C.; Bjørklund, G.; Nguyen, H.V.; Farid, A.; Sochor, J. Effect of biosynthesized silver nanoparticles on bacterial biofilm changes in *S. aureus* and *E. coli*. *Nanomaterials* **2022**, *12*, 2183. [CrossRef] [PubMed]
85. Barros, I.M.D.C.; Leite, B.H.; Leite, C.F.; Fagg, C.W.; Gomes, S.M.; Resck, I.S.; Fonseca-Bazzo, Y.M.; Magalhães, P.O.; Silveira, D. Chemical composition and antioxidant activity of extracts from Erythroxylum suberosum A. St. Hil. leaves. *J. Appl. Pharm. Sci.* **2017**, *7*, 088–094.
86. Urnukhsaikhan, E.; Bold, B.E.; Gunbileg, A. Antibacterial activity and characteristics of silver nanoparticles biosynthesized from Carduus crispus. *Sci. Rep.* **2021**, *11*, 21047. [CrossRef] [PubMed]
87. Li, W.R.; Xie, X.B.; Shi, Q.S.; Zeng, H.Y.; Ou-Yang, Y.S.; Chen, Y.B. Antibacterial activity and mechanism of silver nanoparticles on Escherichia coli. *Appl. Microbiol. Biotechnol.* **2010**, *85*, 1115–1122. [PubMed]

88. Wang, L.S.; Gupta, A.; Rotello, V.M. Nanomaterials for the treatment of bacterial biofilms. *ACS Infect. Dis.* **2015**, *2*, 3–4. [CrossRef] [PubMed]
89. Blango, M.G.; Mulvey, M.A. Persistence of uropathogenic Escherichia coli in the face of multiple antibiotics. *Antimicrob. Agents Chemother.* **2010**, *54*, 1855–1863. [CrossRef] [PubMed]

Disclaimer/Publisher's Note: The statements, opinions and data contained in all publications are solely those of the individual author(s) and contributor(s) and not of MDPI and/or the editor(s). MDPI and/or the editor(s) disclaim responsibility for any injury to people or property resulting from any ideas, methods, instructions or products referred to in the content.